Identification of Transthyretin Tetramer Kinetic Stabilizers That Are Capable of Inhibiting the Retinol-Dependent Retinol Binding Protein 4-Transthyretin Interaction

Christopher L. Cioffi,*† Arun Raja,† Parthasarathy Muthuraman,† Aravindan Jayaraman,† Srinivasan Jayakumar,† Andras Varadi,§ Boglarka Racz,§ and Konstantin Petrukhin*§

†Albany College of Pharmacy and Health Sciences, Departments of Basic and Clinical Sciences and Pharmaceutical Sciences, 106 New Scotland Ave, Albany, NY 12208

§Department of Ophthalmology, Columbia University Medical Center, New York, NY 10032

Abstract: Dissociation of transthyretin (TTR) tetramers may lead to misfolding and aggregation of pro-amyloidogenic monomers, which underlies TTR amyloidosis (ATTR) pathophysiology. ATTR is a progressive disease resulting from the deposition of toxic fibrils in tissues that predominantly presents clinically as amyloid cardiomyopathy and peripheral polyneuropathy. Ligands that bind to and kinetically stabilize TTR tetramers prohibit their dissociation and may prevent ATTR onset. Drawing from clinically investigated AG10, we designed a constrained congener (**18a**) that exhibits excellent TTR tetramer binding potency, prevents TTR aggregation in a gel-based assay, and

possesses desirable pharmacokinetics in mice. Additionally, **18a** significantly lowers murine serum retinol-binding protein 4 (RBP4) levels despite a lack of binding at that protein's all-*trans*-retinol site. We hypothesize that kinetic stabilization of TTR tetramers via **18a** is allosterically hindering all-*trans*-retinol-dependent RBP4-TTR tertiary complex formation and that the compound could present ancillary therapeutic utility for indications treated with RBP4 antagonists, such as macular degeneration.

INTRODUCTION

Transthyretin (TTR, thyroxine binding prealbumin) is a 55 kDa homotetramer comprised of four β-sheet-rich, 127-residue polypeptide monomers that is largely synthesized in the liver for secretion into the blood.[1] TTR tetramers possess two high-affinity binding sites for the thyroid hormone thyroxine (T4, **1**) (Figure 1). However, less than 1% of circulating TTR carries T4 while another serum protein, thyroxine binding globulin (TBG), functions as its primary transporter in the blood.[1] While TTR is not a primary carrier of T4 in the serum, it serves as the major transport protein for the hormone in the central nervous system (CNS) where choroid plexus-derived TTR delivers T4 from the cerebral spinal fluid (CSF) to the choroid plexus and the brain.[2] Accumulating evidence suggests that TTR may play an auxiliary role in sequestering β-amyloid (Aβ) peptides within the CSF by promoting their clearance from the CNS to the periphery, potentially providing neuroprotective effects against Alzheimer's disease (AD).[3-5] In systemic circulation, a significant portion of circulating TTR (approximately 50%) forms a macromolecular complex with retinol binding protein 4 (RBP4) associated with all-*trans*-retinol (vitamin

2

A, **2**).[6, 7] This retinol-dependent RBP4-TTR interaction is essential for efficient systemic trafficking of **2** as it prevents glomerular filtration of the low molecular weight RBP4-all-*trans*-retinol complex (holo-RBP4).[8]
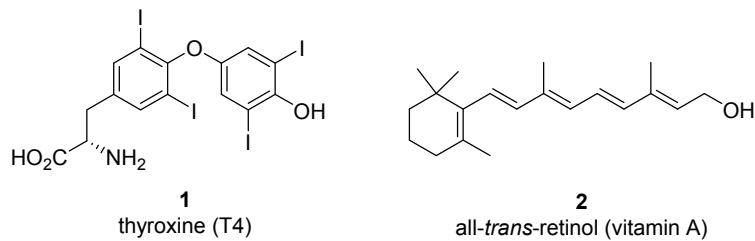

Figure 1. The thyroid hormone thyroxine (T4) (**1**) and all-*trans*-retinol (vitamin A) (**2**).

The circulating TTR molecule is a homotetramer formed by two dimers.[1] To form the homotetrameric structure, two TTR monomers initially associate in a dimer subunit, which further associates with a second dimer subunit. The resulting dimer of dimer architecture presents a tetramer bearing two identical *C2* symmetric T4-binding sites located within a central channel of the tetramer and formed at the dimer-dimer interface.[1] The TTR dimer-dimer interface is relatively weak and its dissociation is the rate-limiting step in the overall TTR tetramer dissociation process.[9] The free dimer subunits may subsequently further dissociate into monomers that could potentially proceed to misfold and oligomerize. Oligomerization can eventually lead to aggregation and formation of toxic amyloid fibrils, which underlies the pathophysiology of TTR amyloidosis (ATTR).[9]

Autosomal dominant ATTR is a rare and progressive disease that involves severe organ damage due to the extracellular deposition of the aforementioned toxic TTR

amyloid fibrils in tissues. The disease typically presents clinically as either TTR amyloid cardiomyopathy (ATTR-CM; can lead to arrhythmias, arterial fibrillation, and biventricular heart failure)[10, 11] or as peripheral polyneuropathy (ATTR-PN; can cause loss of sensation, tingling, numbness, or pain as well as damage to the autonomic nervous system)[12] and can arise from pro-pathogenic monomers with inherited TTR mutations. Non-hereditary ATTR may emerge from wild-type TTR (WT-TTR) monomer misfolding in older individuals.[13] There are at least seventy-seven TTR mutations associated with familial ATTR diseases, and these variants influence amyloidogenicity by either 1) reducing the thermodynamic stability of the TTR tetramer (i.e., the monomers are less likely to associate into a TTR tetramer and are more likely to misfold into an amyloidogenic intermediate), 2) reducing the kinetic barrier for tetramer dissociation (the TTR tetramer with the variant dissociates at a faster rate than WT-TTR with a concomitant increase in monomer aggregation rate), or 3) both thermodynamically and kinetically destabilizing the TTR tetramer.[14] The kinetically stable but thermodynamically destabilized variant V30M[15] is predominantly associated with late-onset familial amyloid polyneuropathy (FAP) and is strongly pathogenic. The most common amyloidogenic TTR variant, V122I,[16] presents at a relatively high frequency within the African-American population (approximately 3.4%) and is predominantly associated with familial amyloid cardiomyopathy (FAC). Its pathogenicity is attributed to its ability to kinetically destabilize the TTR tetramer and induce a dissociation rate that is approximately 2-fold faster than WT-TTR.[17] The L55P mutation both thermodynamically and kinetically destabilizes tetramer formation and can aggressively promote early-onset ATTR-CM and

4

ATTR-PN.[18] Conversely, compound heterozygotes carrying a pro-amyloidogenic TTR mutation (e.g., V30M) and a disease-suppressing mutation that hyperstabilzes TTR tetramers, such as T119M or R104H,[19] are reported to either develop a mild late-onset pathology or be completely protected against ATTR. The T119M variant kinetically stabilizes the TTR tetramer whereas the R104H variant provides thermodynamic stability to the quaternary structure. This difference in mechanism of stabilization is crucial as the T119M variant is resistant to tetramer dissociation and aggregation and provides a greater level of protection against TTR aggregation *in vitro* relative to R104H. Lastly, WT-TTR misfolding and aggregation that occurs non-genetically with age is associated with senile systemic amyloidosis (SSA), a late-onset and prevalent form of ATTR that is estimated to affect 10% to 20% of individuals aged 80 years and older.

Currently available FDA-approved approaches for treating ATTR-CM and ATTR-PN include two treatments that reduce circulating TTR levels (the antisense oligonucleotide inotersen[20] and the small interfering RNA (siRNA) patisiran[21]) and the small molecule tafamidis (vyndaqel and vyndamax, **3**) (Figure 2) that binds to and stabilizes circulating TTR tetramers.[22-27] Ligand binding at the T4 sites has been shown to kinetically stabilize TTR tetramers by increasing the dissociative energy barrier of the native tetrameric state. Due to the presence of two additional T4 transport proteins (TGB and albumin), the majority of TTR in circulation is not bound to TTR and the T4 binding sites are largely unoccupied (>99% unoccupied). Thus, drug discovery approaches to identify T4-competitve small molecules capable of kinetically stabilizing TTR tetramers has garnered significant interest as a therapeutic option for treating ATTR. Numerous structurally

diverse scaffolds in addition to tafamidis have been reported to bind at the T4 site and stabilize TTR tetramers, and representatives of this class are highlighted in Figure 2. The two most advanced small molecule TTR tetramer stabilizers to date include the aforementioned FDA-approved **3** and clinically investigated AG10 (**4**).[28-30] TTR stabilizer **3** has been approved for the treatment of FAP and ATTR-CM. A Phase III study with 441 ATTR-CM patients showed administration of **3** reduced the risk of death by 30% and the rate of cardiovascular-related hospitalizations by 32% compared to placebo controls.[31] TTR stabilizer **4** was reported to be well-tolerated and demonstrated near-complete stabilization of TTR in a 28-day Phase II proof-of-concept trial with ATTR-CM patients presenting symptomatic chronic heart failure.[32] Phase III clinical trials with **4** for the treatment of ATTR-CM and ATTR-PN are currently ongoing. In addition, the repurposed FDA-approved non-steroidal anti-inflammatory drug (NSAID) diflunisal (**5**)[33] and catechol-O-methyl transferase (COMT) inhibitor tolcapone (**7**)[34] are also reported to exhibit TTR tetramer stabilization activity and have been investigated for clinical efficacy against ATTR-PN.
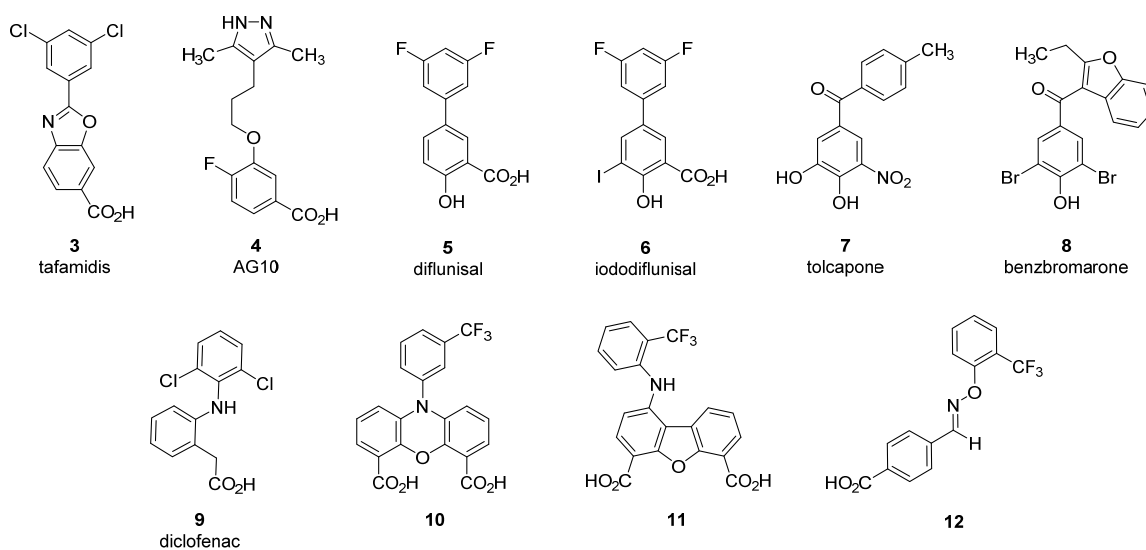
Figure 2. Representative examples of various reported TTR tetramer stabilizer structural classes that bind at the T4 binding site. This sample set of TTR tetramer stabilizers include tafamidis (**3**),[22] AG10 (**4**),[30] diflunisal (**5**),[33] iododiflunisal (**6**),[35] tolcapone (**7**),[34] benzbromarone (**8**), diclofenac (**9**),[36] *N*-phenyl phenoxazine **10**,[37] dibenzofuran **11**,[38] and bisaryloxime ether **12**.[39]

In recent years, the circulating RBP4-TTR-all-*trans*-retinol transport complex has become a target for pharmacological intervention in ophthalmic diseases associated with enhanced accumulation of cytotoxic lipofuscin bisretinoids in the retina. Formation of this transport complex requires that **2** be initially bound to RBP4 as apo-RBP4 poorly associates with TTR.[8] Reports indicate that prevention of RBP4-TTR-all-*trans*-retinol tertiary complex formation can be achieved via selective all-*trans*-retinol-competitive RBP4 antagonists, which leads to a lowering of serum RBP4 facilitated by rapid glomerular filtration due to its relatively low molecular weight (21 kDa).[8] Evidence suggests that pharmacological reduction of serum RBP4 levels via selective RBP4

antagonists holds therapeutic promise for a variety of diverse indications. For example, it has been hypothesized that RBP4 antagonists may provide a mechanism by which to slow or halt the progression of geographic atrophy in dry age-related macular degeneration (AMD) and Stargardt disease patients by impeding ocular influx of **2** and halting the accumulation of cytotoxic lipofuscin bisretinoids in the retina.[40] We have shown that potent and selective RBP4 antagonists disrupt RBP4-TTR-all-*trans*-retinol tertiary complex formation *in vitro* and significantly reduce serum RBP4 levels *in vivo* in rodents and non-human primates.[41-44] Furthermore, chronic oral administration of RBP4 antagonists in *Abca4*$^{-/-}$ knockout mice, a model of excessive lipofuscinogenesis that recapitulates the Stargardt disease phenotype, led to a reduction in retinal cytotoxic bisretinoid accumulation with an ancillary stabilization of a complement system protein expression in the retinal pigment epithelium (RPE).[45, 46] Furthermore, additional dosing studies in wild-type BALB/cJ mice revealed that RBP4 antagonist-induced reductions in circulating RBP4 levels correlated with partial reductions in bisretinoid precursor concentrations without disruption of visual cycle kinetics.[45]

To date, only selective all-*trans*-retinol-competitive antagonists of RBP4 have been reported to block the formation of a tertiary complex with TTR and lead to a reduction in circulating RBP4 levels *in vivo* with concomitant inhibition of bisretinoid synthesis in the retina. While selective RBP4 antagonists can be a safe and effective bisretinoid-lowering therapy for a majority of dry AMD and Stargardt disease patients, this class of compounds may potentially be counter-indicated for a fraction of macular degeneration patients who are predisposed to diseases associated with TTR aggregation. Selective

RBP4 antagonists would release the unliganded TTR tetramer from the circulating RBP4-TTR-all-*trans*-retinol transport complex. It has been previously suggested that the RBP4-TTR-all-*trans*-retinol interaction may stabilize TTR tetramers and the release of a significant pool of unliganded TTR tetramer induced by selective RBP4 antagonists may facilitate TTR amyloid fibril formation in susceptible individuals[14, 15] promoting ATTR diseases.[16-18]

We hypothesized that ligands that selectively bind to TTR tetramers and not to RBP4 may also be capable of antagonizing RBP4-TTR-all-*trans*-retinol tertiary complex formation. Prior to the work reported herein, TTR had not been considered as a drug target for mechanisms or indications that may be treated via RBP4 antagonists. Based on our data, there are TTR ligands that allosterically antagonize retinol-dependent RBP4-TTR interaction. Such ligands would induce the disruption of the RBP4-TTR-all-*trans*-retinol complex with subsequent reduction in serum RBP4 and **2** levels. This would lead to the reduced uptake of **2** to the retina, modulation of the visual cycle and reduction in formation of cytotoxic lipofuscin bisretinoids and bisretinoid precursors. At the same time, such ligands could stabilize TTR tetramers released from the RBP4-TTR-all-*trans*-retinol complex thereby preventing the formation of amyloid fibrils in patients who, in addition to dry AMD and Stargardt disease, may also carry pro-amyloidogenic mutations in the TTR gene.

In our work reported herein, we initiated a structure-based drug design effort to identify a novel class of TTR tetramer kinetic stabilizers that are capable of reducing circulating levels of RBP4 using clinically investigated **4** as a lead. We selected **4** as a

benchmark scaffold from which to develop a novel series of ligands as 1) **4** has been reported to effectively bind at both WT-TTR and the pro-amyloidogenic V122I-TTR variant, and 2) **4** is also reported to be more potent and selective for stabilizing TTR tetramers in buffer and human serum than **3**, despite both compounds exhibiting similar TTR binding affinities (K_d for **4** = 4.8 ± 1.9 nM; K_d for **3** = 4.4 ± 1.3 nM).[29, 30] Our goal was to identify novel chemical matter capable of 1) retaining or improving the observed *in vitro* TTR tetramer binding potency observed for **4**, 2) exhibiting suitable PK properties to allow for adequate TTR tetramer stabilization and prevention of aggregation *in vivo* upon oral administration, and 3) presenting a favorable Absorption Distribution Metabolism and Excretion (ADME) profile and no limiting off-target pharmacology that would inhibit further drug development. In addition, recently published Phase I human PK data for **4** revealed that the major metabolic pathway for the compound involves acyl glucuronidation of its carboxylic acid.[47] Thus, we also sought to include analogues within our sample set that may potentially circumvent this metabolic pathway, which is generally reported to be associated with increased incidences of idiosyncratic toxicity. Our medicinal chemistry strategy utilized available structural data of **4** bound to V122I-TTR (PDB 4HIQ) (*vide infra*)[30] to help design novel scaffolds that 1) maintain or improve the enthalpic contributions to binding observed for **4** that are reported to play a pivotal role in its ability to bind to and kinetically stabilize TTR tetramers (e.g., maintaining pivotal hydrogen bond (H-bond) and van der Waals interactions), and 2) potentially improve entropic contributions to binding by reducing the conformational flexibility

presented by **4**. Compound binding potency to unliganded TTR tetramers for our novel ligands was measured using an established fluorescence polarization assay (FP).[48]

As outlined in Figure 3, our medicinal chemistry plan focused on exploring emerging structure-activity relationship (SAR) trends resulting from alterations to three key regions of lead **4**. This included exploring the SAR of 1) alternative conformationally constrained cyclic core linkers, 2) isosteres and replacements for the 3,5-dimethyl-1*H*-pyrazole "head group region", and 3) variation of substituents and substitution patterns on benzoic acid "bottom group region" appendage. Analysis of PDB 4HIQ suggested that replacing the *n*-propyloxy core linker of **4** with a more conformationally constrained piperazine ring to tether the 3,5-dimethyl-1*H*-pyrazole and the fluorobenzoic acid head and bottom group appendages could potentially provide a binding pose that would align with the observed putative **4** bioactive conformation while being more entropically favorable. Thus, we designed and synthesized illustrative examples of constrained analogues of **4** that initially incorporated a piperazine linker and later included fused bicyclic and spirocyclic piperazine ring isosteres. We subsequently investigated the SAR of a series of analogues that featured a 3,5-dimethyl-1*H*-pyrazole head group with a piperazine core linker while presenting differing benzoic acid substituents. Previously reported SAR campaigns for **4** suggest that positioning the carboxylic acid *meta* to its *n*-propyloxy linker was optimal for electrostatic salt-bridge formation with the Lys 15 and Lys15' residues residing near the periphery of the T4 binding site opening (*vide infra*). Thus, we fixed the carboxylic acid at the same position for our series of analogues while exploring alternative substituents and substitution patterns to the fluorine of **4**. We also

explored the SAR of a small set of isosteres and replacements for the 3,5-dimethyl-1*H*-pyrazole head group of **4**, which projects deep into the T4 binding site and engages in H-bond interactions with Ser117 and Ser117'(*vide infra*). Lastly, we investigated the SAR effects of a carboxylic acid replacement and bioisostere that could mitigate or circumvent potential undesirable acyl glucuronidation metabolism.[49]

SAR Approach Toward Novel TTR Tetramer Kinetic Stabilizers Derived From Benchmark 4

Head Group Region:
Explore pyrazole isosteres and replacements. Explore SAR of alternative motifs capable of interacting with Ser117/Ser117'.

Core Scaffold Region:
Install conformationally contrained piperazine ring and piperazine ring isostere scaffolds that reduce the number of rotatable bonds relative to the core linker of **4**.

Carboxylic Acid Replacement and Bioisostere:
Explore a carboxylic acid replacement and bioisostere that may circumvent acyl glucuronidation reported to be associated with **4** in humans.

Bottom Group Region:
Investigate alternately substituted benzoic acid appendages. Install alternative substituents and vary substitution patterns to explore SAR effects.
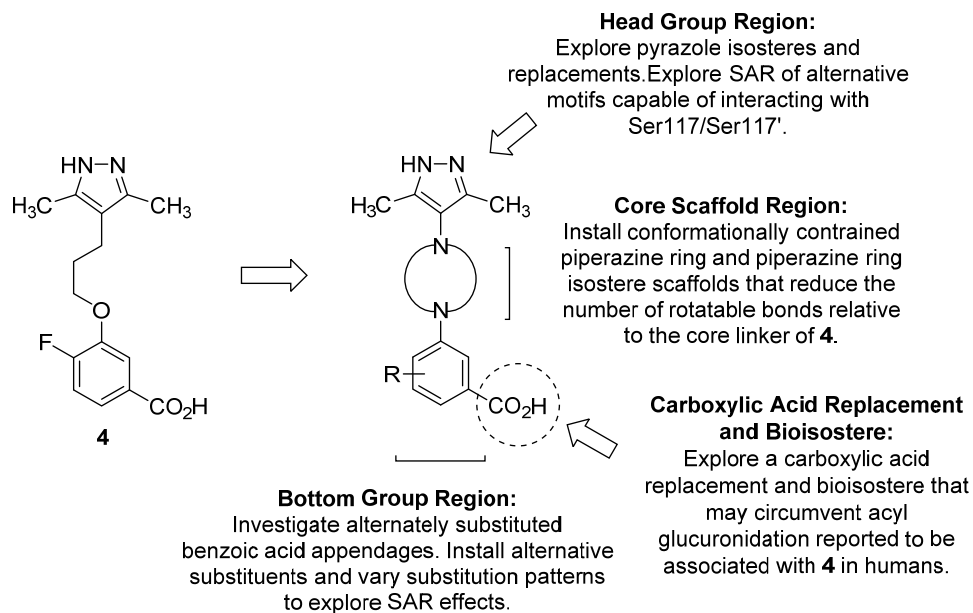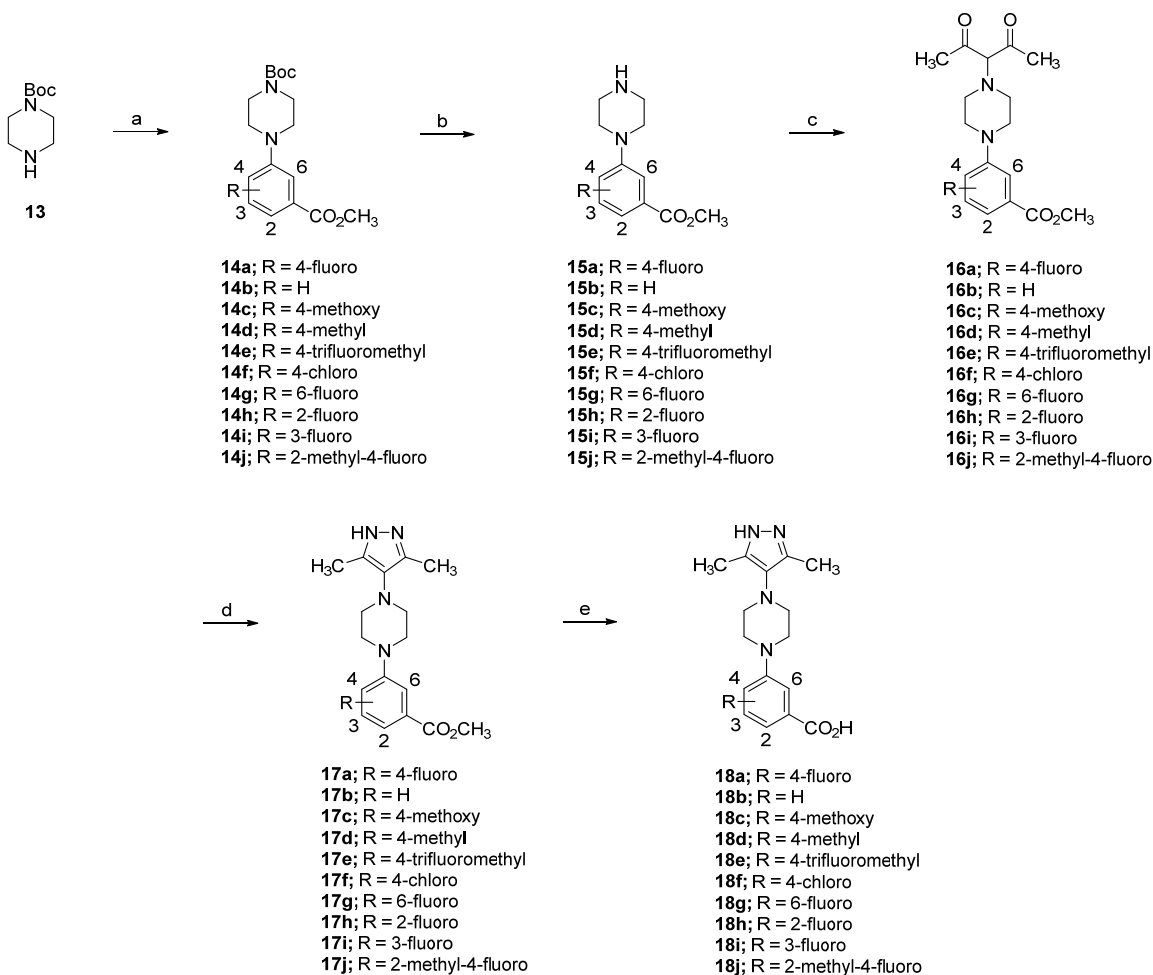
Figure 3. Medicinal chemistry work plan for the identification of novel and conformationally constrained TTR tetramer kinetic stabilizers.

CHEMISTRY

The synthetic route for a series of substituted 3-(4-(3,5-dimethyl-1H-pyrazol-4-yl)piperazin-1-yl)benzoic acid analogues (**18a**-**18j**), highlighted in Scheme 1, begins with

a palladium(0)-catalyzed amination between *tert*-butyl piperazine-1-carboxylate (**13**) and a corresponding substituted methyl bromobenzoate. The resulting aryl amines (**14a**-**14j**) were *N*-Boc deprotected with trifluoroacetic acid (TFA) in CH_2Cl_2 at 0 °C, yielding free amines **15a**-**15j** that were subsequently alkylated with 3-chloropentane-2,4-dione to give the dione intermediates **16a**-**16j**. Diones **16a**-**16j** underwent condensation with hydrazine hydrate ($N_2H_2 \cdot H_2O$) to provide the respective dimethyl pyrazoles **17a**-**17j**, which upon saponification with lithium hydroxide (LiOH) followed by neutralization of the lithium carboxylate salts with 2 N aqueous hydrochloric acid (HCl) yielded the desired carboxylic acids **18a**-**18j**.

Scheme 1[a]

14a; R = 4-fluoro
14b; R = H
14c; R = 4-methoxy
14d; R = 4-methyl
14e; R = 4-trifluoromethyl
14f; R = 4-chloro
14g; R = 6-fluoro
14h; R = 2-fluoro
14i; R = 3-fluoro
14j; R = 2-methyl-4-fluoro

15a; R = 4-fluoro
15b; R = H
15c; R = 4-methoxy
15d; R = 4-methyl
15e; R = 4-trifluoromethyl
15f; R = 4-chloro
15g; R = 6-fluoro
15h; R = 2-fluoro
15i; R = 3-fluoro
15j; R = 2-methyl-4-fluoro

16a; R = 4-fluoro
16b; R = H
16c; R = 4-methoxy
16d; R = 4-methyl
16e; R = 4-trifluoromethyl
16f; R = 4-chloro
16g; R = 6-fluoro
16h; R = 2-fluoro
16i; R = 3-fluoro
16j; R = 2-methyl-4-fluoro

17a; R = 4-fluoro
17b; R = H
17c; R = 4-methoxy
17d; R = 4-methyl
17e; R = 4-trifluoromethyl
17f; R = 4-chloro
17g; R = 6-fluoro
17h; R = 2-fluoro
17i; R = 3-fluoro
17j; R = 2-methyl-4-fluoro

18a; R = 4-fluoro
18b; R = H
18c; R = 4-methoxy
18d; R = 4-methyl
18e; R = 4-trifluoromethyl
18f; R = 4-chloro
18g; R = 6-fluoro
18h; R = 2-fluoro
18i; R = 3-fluoro
18j; R = 2-methyl-4-fluoro

[a]Reagents and conditions: (a) substituted methyl bromobenzoate, XPhos, $Pd_2(dba)_3$, Cs_2CO_3, 1,4-dioxane, reflux, 16 h; (b) TFA, CH_2Cl_2, 0 °C to rt, 16 h; (c) 3-chloropentane-2,4-dione, i-Pr_2NEt, DMF, 0 °C to rt, 16 h; (d) $N_2H_2 \cdot H_2O$ (64-65% in H_2O), CH_3OH, rt, 1 h; (e) (i) LiOH, CH_3OH, THF, H_2O, rt, 16 h; (ii) 2 N aqueous HCl.

Fused bicyclic and spirocyclic piperazine ring isostere analogues of **18a** (**19**-**21**) were prepared and their corresponding syntheses are shown in Scheme 2. The preparation of each analogue of this sample set began with a palladium(0)-catalyzed amination between the corresponding *N*-Boc protected piperazine ring isostere (*tert*-butyl (3aR,6aS)-hexahydropyrrolo[3,4-c]pyrrole-2(1H)-carboxylate, *tert*-butyl 2,7-diazaspiro[4.4]nonane-2-carboxylate, and *tert*-butyl 2,6-diazaspiro[3.3]heptane-2-carboxylate, respectively) and methyl 3-bromo-4-fluorobenzoate. TFA-promoted *N*-Boc deprotection followed by 3,5-dimethyl-1*H*-pyrazole construction was conducted using the same three-step process as outlined in Scheme 1. LiOH-mediated hydrolysis of the corresponding methyl esters followed by neutralization of the carboxylate salts with 2 N aqueous HCl provided the desired piperazine ring isostere analogues **19**-**21**.

Scheme 2[a]
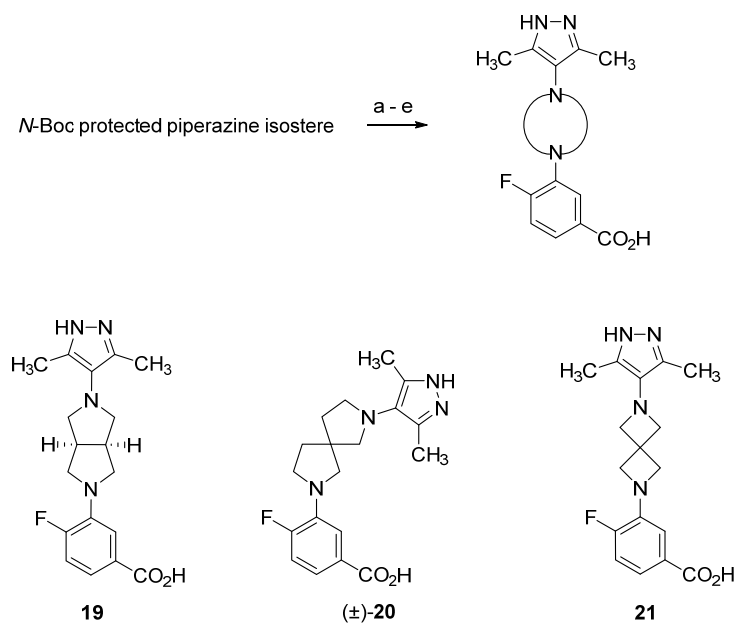
aReagents and conditions: (a) *tert*-butyl (3aR,6aS)-hexahydropyrrolo[3,4-c]pyrrole-2(1H)-carboxylate, *tert*-butyl 2,7-diazaspiro[4.4]nonane-2-carboxylate, or *tert*-butyl 2,6-diazaspiro[3.3]heptane-2-carboxylate, methyl 3-bromo-4-fluorobenzoate, XPhos, Pd$_2$(dba)$_3$, Cs$_2$CO$_3$,1,4-dioxane, reflux, 16 h; (b) TFA, CH$_2$Cl$_2$, 0 °C to rt, 16 h; (c) 3-chloropentane-2,4-dione, *i*-Pr$_2$NEt, DMF, 0 °C to rt, 16 h; (d) N$_2$H$_2$·H$_2$O (64-65% in H$_2$O), CH$_3$OH, rt, 1 h; (e) (i) LiOH, CH$_3$OH, THF, H$_2$O, rt, 16 h; (ii) 2 N aqueous HCl.

The previously described dione intermediate 3-(4-(2,4-dioxopentan-3-yl)piperazin-1-yl)-4-fluorobenzoate (**16a**) also afforded a handle for the construction of isoxazole **23** (Scheme 3), an analogue bearing a 3,5-dimethyl-1*H*-pyrazole head group isostere. Condensation of **16a** with hydroxyl amine hydrochloride (NH$_2$OH·HCl) provided methyl 3-(4-(3,5-dimethylisoxazol-4-yl)piperazin-1-yl)-4-fluorobenzoate (**22**), which was hydrolyzed with LiOH followed by neutralization with 2 N aqueous HCl to give final product 3-(4-(3,5-dimethylisoxazol-4-yl)piperazin-1-yl)-4-fluorobenzoic acid (**23**).

Scheme 3^a
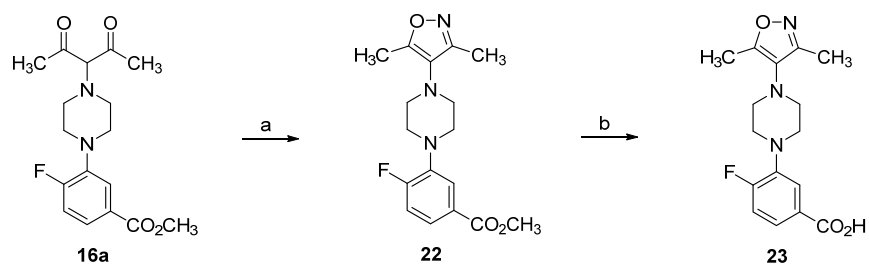
aReagents and conditions: (a) NH$_2$OH·HCl, CH$_3$OH, rt, 16 h; (b) (i) LiOH, CH$_3$OH, THF, H$_2$O, rt, 16 h; (ii) 2 N aqueous HCl.

Scheme 4 presents the routes starting with aryl piperazine intermediate **15a** that enabled preparation of both tetrazole head group analogue **25** and 2-trifluoromethylphenyl head group analogue **27**. Treatment of **15a** with cyanogen bromide (CNBr) at 0 °C in THF in the presence of *N,N*-diisopropylethylamine (*i*-Pr$_2$NEt) afforded an intermediary cyanopiperazine, which underwent cycloaddition with sodium azide (NaN$_3$) in DMF at 120 °C to give tetrazole **24**. Subsequent LiOH saponification of the methyl ester of **24** and neutralization of the lithium carboxylate salt with 2 N aqueous HCl gave desired tetrazole **25**. The preparation of 2-trifluoromethylphenyl analogue **27** began with a palladium(0)-catalyzed amination between **15a** and 1-bromo-2-(trifluoromethyl)benzene to give methyl ester intermediate **26**. Using the aforementioned saponification and neutralization process with **26** afforded desired 2-trifluoromethylphenyl head group analogue **27**.

Scheme 4^a
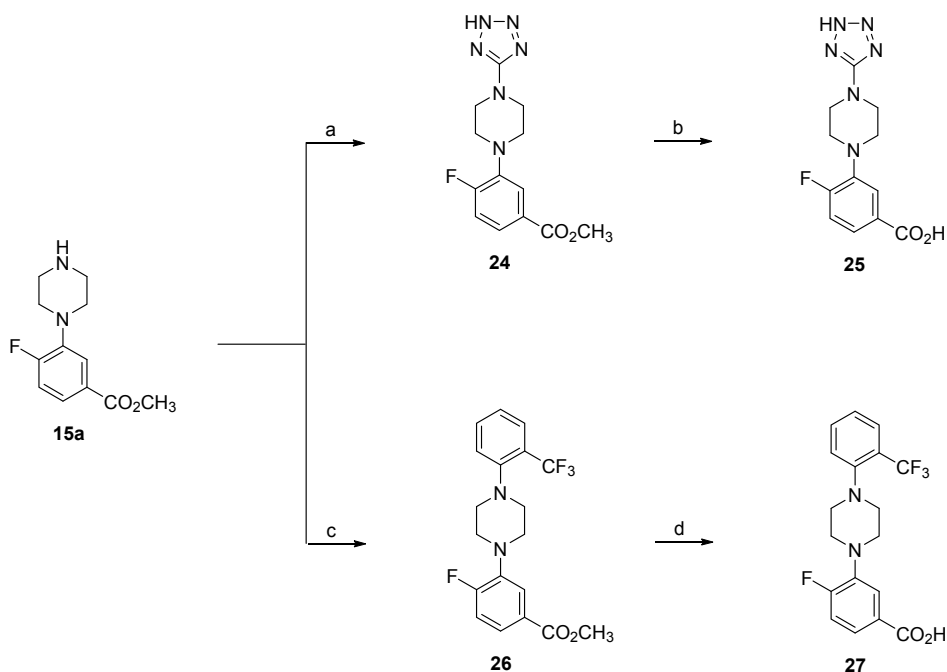
[a]Reagents and conditions: (a) (i) CNBr, *i*-Pr$_2$NEt, THF, 0 °C to rt, 1 h, (ii) NH$_4$Cl, NaN$_3$, DMF, 120 °C, 12 h; (b) (i) LiOH, CH$_3$OH, THF, H$_2$O, rt, 12 h; (ii) 2 N aqueous HCl; (c) 1-bromo-2-(trifluoromethyl)benzene, X-Phos, Pd$_2$(dba)$_3$, Cs$_2$CO$_3$, 1,4-dioxane, reflux, 16 h; (d) (i) LiOH, CH$_3$OH, THF, H$_2$O, rt, 12 h; (ii) 2 N aqueous HCl.

The preparation of the homologated variant of **18a**, analogue **29**, is shown in Scheme 5. A sodium triacetoxyborohydride (NaBH(OAc)$_3$)-mediated reductive amination between amine **15a** and 3-methyl-1*H*-pyrazole-4-carbaldehyde provided methyl ester **28**, which upon saponification and subsequent 2 N aqueous HCl neutralization provided desired homologated analogue **29**.

Scheme 5^a

15a   28   29
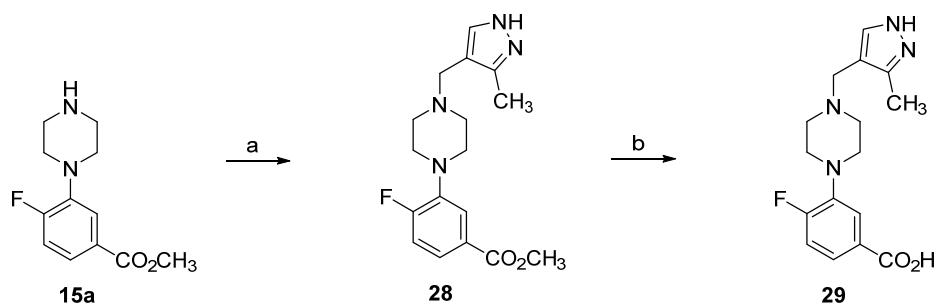
[a]Reagents and conditions: (a) 3-methyl-1H-pyrazole-4-carbaldehyde, NaBH(OAc)$_3$, HOAc, 1,2-dichloroethane, 60 °C, 12 h; (b) (i) LiOH, CH$_3$OH, THF, H$_2$O, rt, 12 h; (ii) 2 N aqueous HCl.

Replacement of the carboxylic acid of **18a** with a primary carboxamide (**30**) and the bioisostere tetrazole (**31**) was also explored (Scheme 6). Production of primary carboxamide **30** involved between amide bond formation between ammonium chloride and **18a** using the peptide coupling agent O-(benzotriazol-1-yl)-N,N,N',N'-tetramethyluronium hexafluorophosphate (HBTU). The bioisostere tetrazole **31** was furnished from **30** using tetrachlorosilane-sodium azide (NaN$_3$). Tetrachlorosilane-mediated dehydration of primary carboxamide **30** afforded the corresponding nitrile *in situ*, which underwent 1,3-dipolar cycloaddition with NaN$_3$ to afford tetrazole **31** in one pot.

Scheme 6[a]

18a   30   31
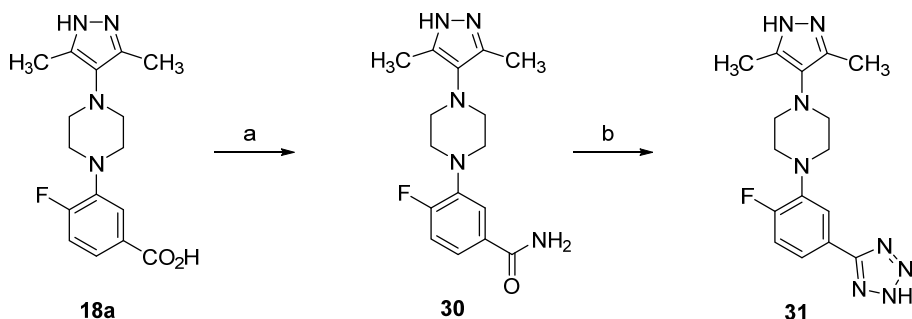
[a]Reagents and conditions: (a) NH_4Cl, HBTU, i-Pr_2NEt, DMF, rt, 18 h; (b) NaN_3, tetrachlorosilane, CH_3CN, 80 °C, 18 h.

RESULTS AND DISCUSSION

We utilized the X-ray crystallographic data PDB 4HIQ in our structure-based drug design efforts, which shows **4** occupying both T4 binding sites of V122I-TTR tetramer (Figure 4, A). Compound **4** was reported to bind to V122I-TTR with negative cooperativity (K_{d1} = 4.8 nM, K_{d2} = 314 nM).[29] The *C2* symmetrical T4 binding sites are subdivided into inner and outer binding cavities containing three pairs of halogen binding pockets (HBP1, HBP1', HBP2, HBP2', HBP3 and HBP3') that the iodine atoms of **1** occupy. Within the innermost region of the T4 binding cavity reside residues Ser117 and Ser117', which engage in bridging hydrogen bond interactions with a resident structural water molecule. These residues are within close proximity to the T4 inner binding cavity HBP3 and HBP3' pockets. The lipophilic HBP2 and HBP2' pockets are located between the inner and outer binding cavities and the HBP1 and HBP1' pockets are housed near the outer region of the binding cavity. The ionizable residues Lys15/Lys15' and Glu54/Glu54' reside near the periphery of the T4 binding site opening.

20

The occupancy of **4** within the T4 site involves a forward binding mode, with the 3,5-dimethyl-1*H*-pyrazole group projecting deep within the inner cavity where it engages in two H-bond interactions with Ser117 and Ser117' (Figure 4, B and C).[29, 30] The two pyrazole methyl groups occupy the neighboring HBP3 and HBP3' pockets where they engage in van der Waals and hydrophobic interactions with the methyl and methylene groups of Ser117/Ser117', Thr119/Thr119', and Leu110/Leu110'. The *n*-propyloxy linker of **4** resides within the center of the binding site channel where it makes van der Waals contacts with the residues lining HBP2 and HBP2', which include Leu110/Leu110', Ala109/Ala109', Lys15/Lys15', and Leu17/Leu17' sidechains. The fluorine atom of the benzoic acid fragment of **4** is *para* to the carboxylic acid and extends into the lipophilic HBP1 pocket, where it makes van der Waals contacts with the aliphatic residues of Ala108 and Val121 and the methyl and methylene groups of Lys15/Lys15' and Thr106/Thr106' (Figure 4, B and C).[29, 30] The carboxylic acid of **4** is positioned in close proximity to the opening of the T4 binding site where it engages in salt-bridge interactions with the ε-amino groups of Lys15 and Lys15'. These ionic binding interactions induce partial closure of the T4 binding site opening and effectively shield bound **4** from solvent.[29, 30]
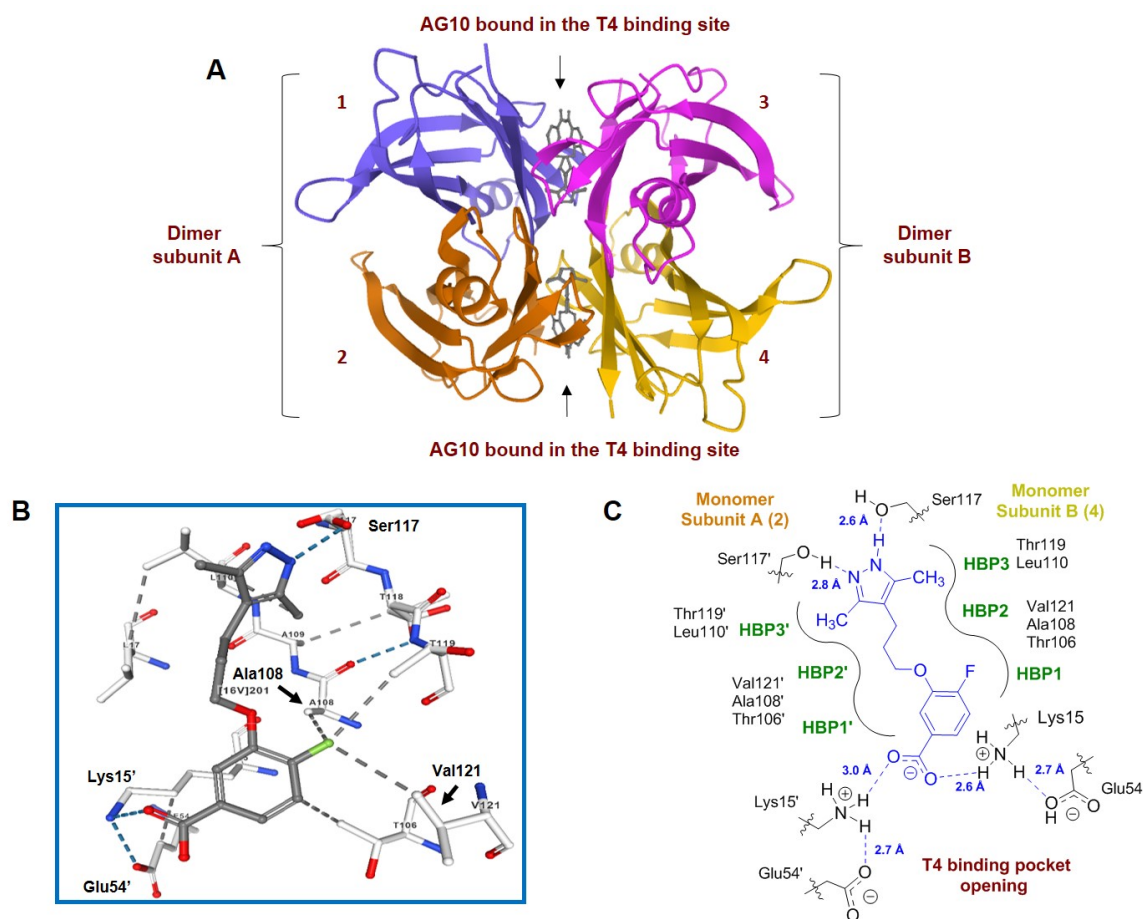
Figure 4. X-ray crystallographic data showing **4** bound to V122I-TTR (PDB 4HIQ). (A) Ribbon

diagram of the quaternary homotetrameric structure of TTR with **4** bound in the T4 binding sites

with both symmetry-related binding conformations shown. The TTR dimers are shown as dimer

subunit A and dimer subunit B and each monomer subunit of the tetramer (labeled 1, 2, 3 and 4)

is shown with its secondary structural elements and colored differently. The monomer

components of dimer A are shown in cyan (monomer 1) and orange (monomer 2). The

monomer components of dimer B are shown in pink (monomer 3) and yellow (monomer 4). The

dimers are associated back-to-back creating a large channel through the center of the tetramer

that presents two *C2* symmetrical T4-binding sites. Compound **4** is shown in stick format (grey).

(B) TTR tetramer kinetic stabilizer **4** is shown in ball and stick format (dark grey) with contacting

residues labeled and illustrated in stick format (white). The binding pose of **4** positions the benzoic acid motif bent out of the plane with the rest of the molecule in a nearly orthogonal orientation. (C) A Ligand interaction diagram of **4** (shown as blue) derived from PDB 4HIQ, which features the HBPs with their associated localized amino acids. The diagram further illustrates key binding interactions observed in the X-ray crystallographic data, including pivotal H-bonds and salt-bridge interactions. The pyrazole head group of **4** projects deep within the inner binding cavity of the T4 binding pocket where it engages in two H-bond interactions with Ser117 and Ser117'. The pyrazole 3,5-dimethyl groups of **4** occupy HBP3 and HBP3'. The aliphatic chain of **4** comes in contact with the residues lining HBP2/HBP2'. The fluorine atom of **4** projects into a hydrophobic region of HBP1 in the outer T4 binding cavity. The carboxylic acid of **4** forms two ionic salt-bridges with the ε-amino groups of Lys15 and Lys15'. The H-bonds and ionic salt-bridge interactions are depicted as blue dashed lines, with the atomic distances labeled in Å.

The reported isothermal titration calorimetry (ITC) thermograms for **3** and **4** show that although both compounds present similar changes in Gibbs free energy of binding (ΔG; where $\Delta G = \Delta H - T\Delta S$) ($\Delta G$ for **4** = -11.34 kcal/mol; ΔG for **3** = -11.34 kcal/mol), the compounds differed significantly with regard to their relative enthalpic and entropic contributions.[29, 30] The binding of **4** was found to be largely enthalpically driven (ΔH = -13.60 kcal/mol and $T\Delta S$ = -2.26 kcal/mol) while **3** demonstrated equal enthalpic and entropic contributions to binding (ΔH = -5.00 kcal/mol and $T\Delta S$ = 6.39 kcal/mol). The larger enthalpic contribution for **4** is attributed to the H-bond interactions between its pyrazole head group and Ser117 and Ser117', which are not present for **3**. Importantly, these additional H-bond interactions of **4** with Ser117 and Ser117' appear to mimic the

direct H-bond interaction observed between these two residues in the T119M-TTR disease-suppressing variant.[29, 30] The Ser117 and Ser117' residues of T119M-TTR are within close proximity (~2.8 Å) to form an intramolecular H-bond interaction between them. This pivotal H-bond interaction helps to draw the dimer subunits closer and fortifies the aggregate molecular interactions between them. This is hypothesized to significantly increase in the T119M-TTR dimer-dimer dissociation energy barrier, thus providing superior kinetic stabilization relative to WT-TTR quaternary structure, which does not contain this key Ser117/Ser117' H-bond interaction. Indeed, the T119M variant displays a 40-fold slower dissociation rate relative to WT-TTR. Thus, the ability of **4** to mimic this critical Ser117/Ser117' binding interaction of T119-TTR may explain why it demonstrates superior potency to **3** with regard to stabilizing TTR tetramers in buffer and human serum despite exhibiting a similar binding affinity.[29, 30] Therefore, we endeavored to retain these important enthalpic Ser117/Ser117' H-bond and Lys15/Lys15' salt-bridge interactions in our novel analogue designs.

Structure-Activity Relationships. The less favorable entropic binding energy observed with the ITC thermogram of **4** relative to **3** (**4** $T\Delta S$ = -2.26 kcal/mol; **3** $T\Delta S$ = 6.39 kcal/mol)[29, 30] may potentially be attributed to the conformational flexibility of the *n*-propyloxy core linker, which contains five rotatable bonds. Thus, our initial goal was to prepare a conformationally constrained congener of **4** by installing a piperazine ring as a replacement for the *n*-propyloxy linker. We hoped to potentially further improve potency relative to **4** by maintaining its key enthalpic contributions to binding while ameliorating a putative entropic penalty by reducing the number of rotatable bonds

within the molecule's linker region. Analysis of PDB 4HIQ suggested that a piperazine ring could serve a suitable linker presenting a similar length as the *n*-propyloxy core linker of **4** that can rigidify the observed putative bioactive conformation and effectively project a 3,5-dimethyl-1*H*-pyrazole head group deep within the T4 inner binding cavity while also presenting the carboxylic acid in suitable position for electrostatic salt-bridge formation with Lys15 and Lys15' near the opening of the binding site. In addition, while the piperazine ring does eliminate three rotatable bonds, it still permits the 3,5-dimethyl-1*H*-pyrazole and benzoic acid appendages to adopt the slightly orthogonal orientation they appear to present relative to one another in PDB 4HIQ. Indeed, piperazine **18a** did exhibit excellent potency at TTR (FP IC_{50} = 220 nM) that was approximately 2-fold better than **3** (FP IC_{50} = 410 nM) and comparable to that of **4** (FP IC_{50} = 160 nM) (Table 1). The improved potency relative to **3** suggests that **18a** may also be benefiting from increased enthalpic contributions to binding via putative H-bonds between its pyrazole head groups and Ser117/Ser117'. The lack of improvement in potency of **18a** relative to **4** may be attributed to several factors. For example, potential entropic benefits for binding gained by **18a** may be slightly offset by subtle adverse changes to enthalpic contributions. It is possible that the more electron-rich pyrazole head group of **18a** presents a slightly weaker H-bond donating group relative to the pyrazole of **4**, which could affect the strength of the Ser117/Ser117' H-bond interaction. Furthermore, replacing the aryl ether of **4** with the aryl amine of **18a** may alter the pK_a of the carboxylic acid and modulate the strength of the salt-bridge interaction with Lys15/Lys15'. Additionally, **18a** may be unable to attain a fully suitable bioactive

conformation to allow for optimal pyrazole head group and/or carboxylic acid bottom group binding interactions due to the reduced flexibility of the piperazine linker. The lack of flexibility of the piperazine core may actually not confer a significant entropic benefit and may prevent optimal occupancy of **18a** required for fortified H-bond, van der Waals, and hydrophobic effect contributions. Lastly, it may also be possible that the potencies exhibited by **4** and **18a** may simply represent the upper limit for ligand binding affinity at the T4 site. Future binding affinity, ITC, and X-ray crystallographic data for **18a** will help provide a better understanding of the nature of the compound's binding profile relative to that of **4** and **3**. Lastly, **18a** demonstrated good selectivity over RBP4 as it was found to be inactive in the *in vitro* RBP4 scintillation proximity (SPA) assay (RBP4 SPA IC$_{50}$ > 3 μM), which is used to measure binding potency of all-*trans*-retinol competitive ligands at RBP4.

With **18a** in hand, we next sought to explore the SAR effects of varying the substituents and substitution patterns of the benzoic acid bottom group motif. We prepared a focused sample set of follow-up analogues to **18a** that replaced its *para*-fluorine atom with alternative atoms/groups of increasing size and lipophilicity that might better occupy the neighboring hydrophobic HBP1 pocket, stabilize a putative forward binding pose, and potentially further improve potency (**18c**-**18f**). With the exception of des-fluoro analogue **18b** (FP IC$_{50}$ = 780 nM), the analogues of this sample set all exhibited potencies within a 2-fold range of **18a**. Indeed, *para*-substituted analogues **18c**-**18f** are equipotent to **18a** and appear to provide suitable substituents

capable of occupying HBP1 and engaging in putative favorable van der Waals binding interactions.
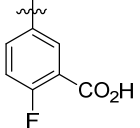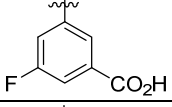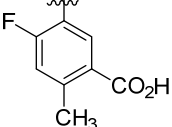
We next investigated whether moving the fluorine of **18a** from the *para* position relative to the carboxylic acid to the corresponding *ortho* and *meta* positions would have an effect on TTR potency (**18g**-**18i**). Interestingly, the SAR for this group demonstrated a preference for fluorine substitution *para* to the carboxylic acid. The *ortho*-fluorinated analogue **18g** exhibited a >2-fold loss in potency relative to **18a** (FP IC_{50} = 550 nM), while the alternate *ortho*-substituted fluorinated analogue **18h** exhibited a greater loss in potency (~6.5-fold) (FP IC_{50} = 1.44 μM). The *meta*-fluoro analogue **18i** (FP IC_{50} = 620 nM) was nearly equipotent with **18g**. The relatively modest decrease in potency observed for **18g** and **18i** may be attributed to their respective fluorine atoms being unable to optimally project into and fully occupy the HBP1' or HBP1 pocket, potentially leading to weaker van der Waals interactions and destabilized binding poses. Contrarily, the substitution pattern of **18h** may potentially project the fluorine atom into an area that does not allow it to occupy either HBP1 or HBP1' and/or engage in any favorable binding interactions, thus leading to the more significant loss in potency exhibited. Lastly, we prepared and tested the di-substituted analogue **18j** that incorporated a methyl group *ortho* (2-position) to the carboxylic acid, which could serve as a potential blocking group to hinder a possible acyl glucuronidation metabolic pathway. Gratifyingly, the compound was active and exhibited good potency (FP IC_{50} = 600 nM). As previously stated, uridine 5'-diphospho-glucuronosyltransferase (UGT) acylglucuronidation has been identified as the predominant metabolic pathway of **4**.[47]

As acyl glucuronidation is reported to be associated with an increased incidence of idiosyncratic toxicity,[49] the diminishment or elimination of this metabolic pathway should be considered during the early stages of drug discovery to potentially remove or hinder the probability of encountering this liability. Although **4** has been found to be safe and well-tolerated clinically, we wanted to investigate early-stage analogues that may potentially hinder an acyl glucuronidation metabolic pathway for our series. Thus, the introduction of a methyl group within close proximity to the nucleophilic carboxylate moiety was anticipated to sterically encumber and reduce its accessibility to UGT and the UDP-glucuronic acid cofactor, potentially impairing or prohibiting acyl glucuronidation.[50] Future metabolite profiling and structural elucidation studies will be conducted to investigate whether or not **18a** and/or **18j** are subject to acyl glucuronidation *in vivo* and if there are significant differences observed with regard to the extent of this type of metabolism between the two analogues.

Table 1. TTR fluorescence polarization and RBP4 SPA binding affinity data for piperazine analogues of **4** bearing various benzoic acid substituents (bottom group region).
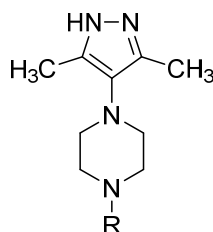
Compound	Benzoic Acid Bottom Group Motif (R)	TTR FP[a] IC$_{50}$ (µM)[c]	RBP4 SPA[b] IC$_{50}$ (µM)[c]
Tafamadis (3)	---	0.41	>30
AG10 (4)	---	0.16	>30
18a		0.22	>3
18b		0.78	>30
18c		0.30	>3
18d		0.21	>3
18e		0.26	>3
18f		0.20	>3
18g		0.55	>3

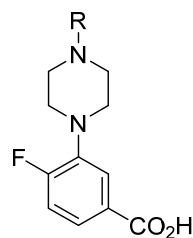|			
18h		1.44	>3
18i		0.62	>3
18j		0.60	>3

[a]IC$_{50}$ values for the FP assay obtained in the presence of a fixed, 25 µM concentration of fluorescein isothiocyanate (FITC)-coupled TTR FP probe. [b]IC$_{50}$ values for the SPA assay obtained in the presence of a fixed, 10 nM concentration of ^{3}H-retinol. [c]For compounds tested multiple times (more than twice) the IC$_{50}$ data is represented as the mean ± standard deviation. For those compounds that were only tested twice, the IC$_{50}$ data is shown as the mean of two independent experiments and not as the mean ± standard deviation. ND = Not determined.

We next explored the SAR effects of a focused sample set of three piperazine ring isostere core linker analogues (Table 2). The (3as,6as)-octahydropyrrolo[3,4-c]pyrrole fused bicyclic analogue **19** exhibited an order of magnitude loss in potency relative to **18a** (FP IC$_{50}$ = 2.82 µM), while racemic 2,7-diazaspiro[4.4]nonane (±)-**20** was found to be 5-fold less potent (FP IC$_{50}$ = 1.08 µM). 2,6-Diazaspiro[3.3]heptane **21** was inactive at TTR. None of the piperazine isostere analogues demonstrated activity in the *in vitro* RBP4 SPA assay. The diminishment in potency or complete loss of activity for these compounds could be attributed to either the longer lengths or unfavorable geometries

(or both) of the linkers, which prohibited the formation of compatible binding poses within the T4 site.

Table 2. TTR fluorescence polarization and RBP4 SPA binding affinity data for additional conformationally constrained core analogues.
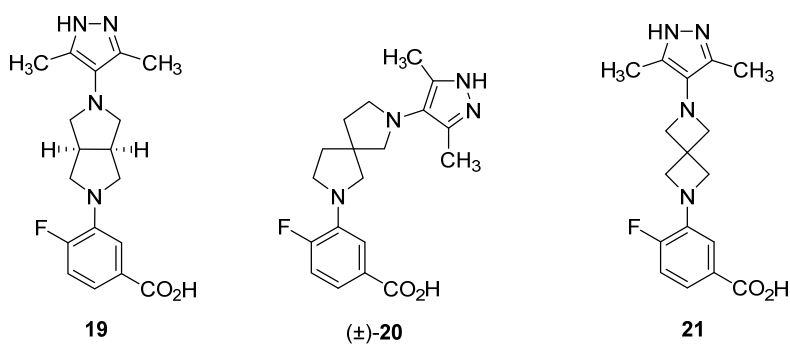
Compound	TTR FP[a] IC$_{50}$ (μM)[c]	RBP4 SPA[b] IC$_{50}$ (μM)[c]
18a	0.22	>3
19	2.82	>3
(±)-20	1.08	>3
21	>30	>3

[a]IC$_{50}$ values for the FP assay obtained in the presence of a fixed, 25 μM concentration of fluorescein isothiocyanate (FITC)-coupled TTR FP probe. [b]IC$_{50}$ values for the SPA assay obtained in the presence of a fixed, 10 nM concentration of ^{3}H-retinol. [c]For compounds tested multiple times (more than twice) the IC$_{50}$ data is represented as the mean ± standard deviation. For those

compounds that were only tested twice, the IC_{50} data is shown as the mean of two independent experiments and not as the mean ± standard deviation. ND = Not determined.

A concise exploration of 3,5-dimethyl-1*H*-pyrazole head group SAR for analogue **18a** was also conducted (**23**-**29**) (Table 3). Previous reports indicate very tight SAR for this region as exchanging the methyl groups of the 3,5-dimethyl-1*H*-pyrazole of **4** with ethyl groups or methylation of one of the pyrazole nitrogen atoms was not well-tolerated.[29] Thus, we prepared a focused sample set that was designed to further probe the nature of the T4 inner binding cavity. Replacement of the 3,5-dimethyl-1*H*-pyrazole of **18a** with a 3,5-dimethylisoxazole ring (**23**) was not well-tolerated and lead to a >20-fold loss in potency (FP IC_{50} = 5.3 μM). This observation may be attributed to the installation of a poorer H-bond accepting isoxazole ring system, which may have led to significantly weaker putative H-bonds with Ser117 and Ser117' relative to **18a**. Incorporation of a tetrazole group (**25**) led to a complete loss in TTR activity, which may be attributed to 1) the contrasting polarity of the tetrazole with the hydrophobic macromolecular interior of the inner T4 binding site, and/or 2) the lack of pendant methyl groups to occupy the adjacent HBP3 and HBP3' pockets. Replacing the 3,5-dimethyl-1*H*-pyrazole of **18a** with a 2-trifluoromethylphenyl head group (**27**) also led to a diminishment in potency (FP IC_{50} = 1.7 μM), though not as severe as was observed for isoxazole **23** and tetrazole **25**. Although **27** is incapable of H-bond interactions with Ser117 and Ser117', its relatively moderate loss in potency within this sample set may be due to 1) better dielectric compatibility between the 2-trifluoromethylphenyl ring and the macromolecular

32

interior of the inner T4 binding site, and/or 2) HBP3/HBP3' pocket occupancy by the lipophilic *ortho*-trifluoromethyl group. The homologated analogue of **18a** (**29**) was found to be in active, possibly due unfavorable alignment of the pyrazole head group within the T4 binding site as a result of the methylene extension of the scaffold.

Table 3. TTR fluorescence polarization and RBP4 SPA binding affinity data for analogues bearing 3,5-dimethyl-1*H*-pyrazole replacements (head group region).
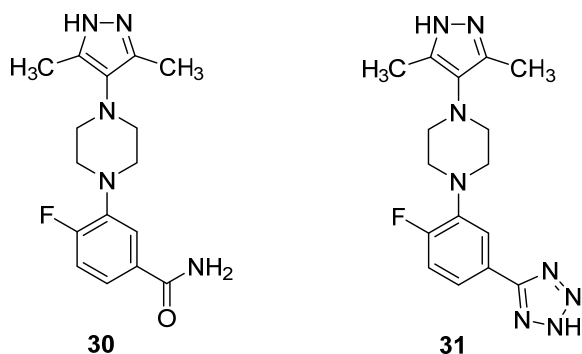

Compound	Head Group (R)	TTR FP[a] IC_{50} $(\mu M)^{c}$	RBP4 SPA[b] IC_{50} $(\mu M)^{c}$
18a	HN-N H3C CH3	0.22	>3
23	O-N H3C CH3	5.3	>3
25	HN-N N N	>30	>3
27	CF3	1.7	>3
29	NH N CH3	>30	>30

We then examined two replacements for the carboxylic acid of **18a**, which included primary carboxamide **30** and the bioisostere tetrazole **31**. Carboxamide **30** exhibited good potency and was approximately 3-fold less potent than **18a**. This is presumably due to the fact that the primary carboxamide, although capable of serving as an H-bond donor and acceptor that can form strong charge-reinforced H-bonds with Lys15/Lys15' and Glu54/Glu54', is non-ionizable and unable to engage in stronger ionic salt-bridge interactions. The tetrazole of **31** is ionizable at physiological pH and serves as a suitable bioisostere of the carboxylic acid of **18a**, thus likely allowing it to participate in salt-bridge interactions with Lys15/Lys15', which may explain why it is equipotent with **18a**. As an additional beneficial attribute, the tetrazole of **31** may also serve to potentially hinder acyl glucuronidation.

Table 4. TTR fluorescence polarization and RBP4 SPA binding affinity data for primary carboxamide and tetrazole analogues (bottom group region).

Compound	TTR FP[a] IC$_{50}$ (μM)[c]	RBP4 SPA[b] IC$_{50}$ (μM)[c]
18a	0.22	>3
30	0.67	>3
31	0.26	>3

[a]IC$_{50}$ values for the FP assay obtained in the presence of a fixed, 25 μM concentration of fluorescein isothiocyanate (FITC)-coupled TTR FP probe. [b]IC$_{50}$ values for the SPA assay obtained in the presence of a fixed, 10 nM concentration of ^{3}H-retinol. [c]For compounds tested multiple times (more than twice) the IC$_{50}$ data is represented as the mean ± standard deviation. For those compounds that were only tested twice, the IC$_{50}$ data is shown as the mean of two independent experiments and not as the mean ± standard deviation. ND = Not determined.

Analogue **18a** emerged as a lead upon completion of our SAR campaign and was further evaluated for its ADME properties. The *in vitro* pharmacological profile

presented in Table 5 shows that **18a** possesses excellent kinetic aqueous solubility in phosphate buffered saline (PBS) (pH = 7.4), excellent microsomal stability with low CL_{int} values across multiple species, and % plasma protein binding (PPB) values that indicate relatively low fraction unbound in human, rat, and mouse. In addition, **18a** did not demonstrate any limiting off-target pharmacology in a standard CYP inhibition panel, at the hERG channel, or at the nuclear peroxisome proliferator-activated receptor-gamma (PPARγ) receptor. Analogues from our previously reported RBP4 antagonist series exhibited undesirable ancillary agonist activity at PPARγ, which is why we surveilled our novel TTR tetramer kinetic stabilizer series for this potential off-target pharmacology.[48]

Table 5. *In vitro* ADME profile for **18a**.

Solubility[a]	Microsomal CL_{int} (µL/min/mg)[b]				Liver Microsomal Stability (% remaining at 30 min)[c]				CYP Inhibition (% inhibition at 10 µM) 2C9, 2C19, 2D6, 3A4	hERG[d] (IC_{50})	PPARγ (EC_{50})	%PPB[e]		
	H	R	M	cyno	HLM	RLM	MLM	cyno LM				H	R	M
184.5 µM	<0.0231				93	98	102	94	2C9 – 10.4% 2C19 – 3.1% 2D6 – 8.1% 3A4 – (-)2.2%	>30 µM	>100 µM	83	97	93

[a]Kinetic solubility measured in PBS (pH= 7.4). [b]Microsomal intrinsic clearance (CL_{int}); H = human; R = rat; M = mouse; cyno = cynomolgus monkey. [c]Liver microsomal metabolic stability, % of parent drug remaining after a 30 minute incubation in the presence of the microsomes; HLM = human liver microsomes; RLM = rat liver microsomes; MLM = mouse liver microsomea; cyno LM = cynomolgus monkey liver microsomes. [d]CiPA hERG QPatch Assay; compounds were tested (n = 2) in a five-point concentration-response study. [e]%PPB = plasma protein binding; H = human, R = rat, M = mouse.

In Vivo **Activity: PK characteristics of 18b in mice.** The PK properties of **18a** were determined via studies conducted with CD-1 male mice (2 mg/kg IV and 5 mg/kg PO) (Table 6). The compound exhibited favorable plasma clearance (0.354 L/hr/kg) and a good half-life of 5.08 h. Rapid oral absorption was observed (T_{max} = 0.42 h) with a maximal concentration (C_{max}) of 1563 ng/ml. Compound **18a** presented a low volume of distribution (V_{ss} = 2.19 L/kg), good overall exposure (AUC_{INF} was 16073 hr·ng/mL), and excellent oral bioavailability (%F = 103%). The observed slightly >100% oral bioavailability for **18b** may be the result of its low plasma clearance and potential nonlinear pharmacokinetics over the dose range tested.

Table 6. *In vivo* PK Data for analogue **18a** following IV and PO administration in CD-1 mice.

Route	Dose	$C_0{}^a$ (ng/ml)	CL^b (L/hr/kg)	$t_{1/2}{}^c$ (h)	$V_{ss}{}^d$ (L/kg)	$AUC_{last}{}^e$ (hr·ng/mL)	$AUC_{INF}{}^f$ (hr·ng/mL)	$\%F^i$
IV	2 mg/kg	1622 (267)	0.354 (0.139)	5.08 (0.814)	2.18 (0.585)	6214 (2321)	6242 (2303)	NA
Route	**Dose**	$C_{max}{}^g$ (ng/ml)	$T_{max}{}^h$ (h)	$t_{1/2}{}^c$ (h)	$V_{ss}{}^d$ (mL/kg)	$AUC_{last}{}^e$ (hr·ng/mL)	$AUC_{INF}{}^f$ (hr·ng/mL)	$\%F^i$
PO	5 mg/kg	1563 (115)	0.42 (0.14)	5.38 (0.624)	NA	16040 (2778)	16073 (2783)	103 (17.8)

Data are represented as the mean with standard deviation in parentheses (mean (SD)). Dosing groups consisted of three drug naïve adult male CD-1 mice. IV administration: Test article was administered at the 2 mg/kg dose; test article vehicle = 3% DMA/45% PEG300/12% Ethanol/40% Sterile water; PO administration: test article was administered at the 5 mg/kg dose, vehicle = 2 % Tween 80 in 0.9% saline. [a]Observed initial concentration of compound in blood at time zero.

[b]Total body clearance. [c]Apparent half-life of the terminal phase of elimination of compound from blood. [d]Volume of distribution at steady state. [e]Area under the blood concentration versus time curve from 0 to the last time point that compound was quantifiable in blood. [f]Area under the blood concentration versus time curve from 0 to infinity. [g]Maximum observed concentration of compound in blood. [i]Time of maximum observed concentration of compound in blood. [f]Bioavailability; F = (AUC_{INFpo} × $Dose_{iv}$) ÷ AUC_{INFiv} × $Dose_{po}$).

Analogue 18a inhibits formation of high molecular weight forms of TTR. The ability of TTR ligands to act as kinetic stabilizers of TTR tetramers can be assessed *in vitro* using a low pH-induced TTR aggregation SDS-PAGE assay.[24, 25] A 72 h incubation of TTR tetramers at pH = 4.0 initiates its dissociation into monomeric intermediates that misassemble and oligomerize into amyloid fibrils and other high molecular weight forms.[26] To confirm the ability of analogue **18a** to act as a kinetic stabilizer of TTR tetramers, we tested its ability to suppress low pH-mediated TTR aggregate formation using the previously published protocol.[27, 48] FDA-approved **3** was used as a positive control in the aggregation experiments. As shown in Figure 5A, following 72 h of incubation of TTR tetramers with DMSO at pH = 4 at 37 °C, the amount of high molecular weight forms of TTR are greatly increased in comparison to the DMSO control incubated for 72 h at pH = 7.5. Consistent with its ability to act as a kinetic TTR stabilizer, treatment with analogue **18a** (50 μM) as well as with **3** (50 μM), significantly inhibited the formation of high molecular weight forms of TTR (Figure 5, A). Higher intensities of the TTR monomer and dimer bands in samples treated with **18a** and **3** when compared to DMSO correlated with a corresponding reduction in TTR aggregates induced by **18a**

and **3**. Quantification of Western blot band intensities established a 3.1-fold reduction in the amount of aggregates in the presence of **18a** while a 3.0-fold reduction was induced by **3** (Figure 5, B). Significant increase in the dimer band intensities and appreciable increase in the intensity of TTR monomer bands conferred by **18a** and **3** were associated with inhibition of the low pH-induced TTR aggregate formation. (Figure 5, C and D). The results of the conducted aggregation experiments confirmed that **18a** can act as a TTR tetramer kinetic stabilizer.
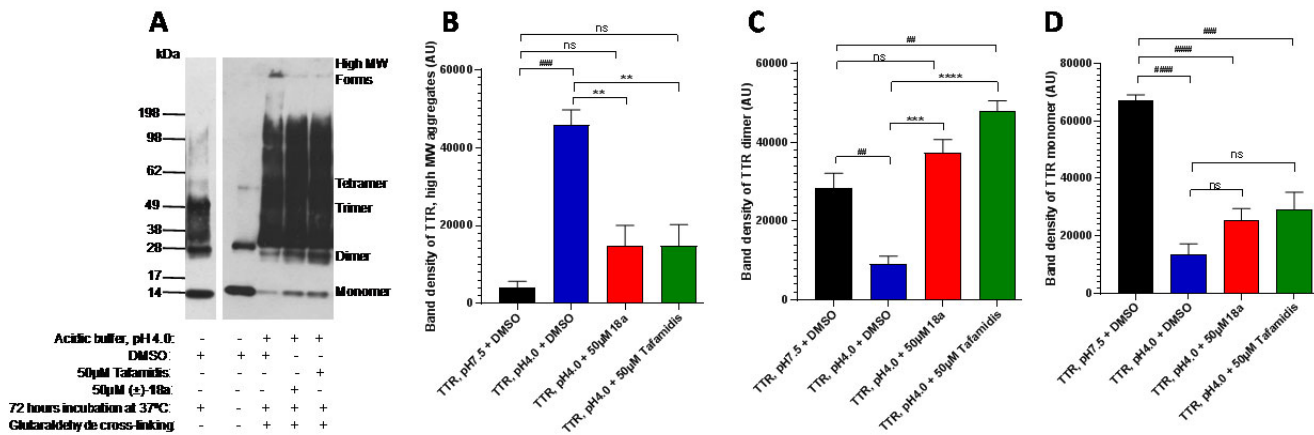

Figure 5. Analogue 18a reduces the formation of high molecular weight TTR forms in the acid-induced aggregation assay. TTR protein (5 μg) was aggregated by using acetate buffer (pH = 4.0) and incubated for 72 h at 37 °C. TTR tetramer concentration during the incubation was 9 μM. After incubation in the presence of DMSO, 50 μM **3** (tafamidis), and 50 μM **18a** and cross-linking with glutaraldehyde, samples were subjected to SDS-PAGE followed by Western blot analysis of TTR. The representative blot of at least three independent experiments is presented (A). Bar graphs represent pixel volume means ± S.D. of the scanned bands on the immunoblots in arbitrary units for TTR high-molecular-weight aggregates (B), dimers (C), and monomers (D).

Statistical significance was determined by one-way ANOVA with Holm-Sidak post hoc test; *, p ≤0.05; **, p ≤0.01; ***, p ≤0.001; ****, p ≤0.0001 compared to TTR aggregation + DMSO group (pH4.0); [#], p ≤0.05; [##], p ≤0.01; [###], p ≤0.001; [####], p ≤0.0001 compare to TTR without aggregation group (pH = 7.5).

***In vivo* activity: RBP4 lowering and PK-PD correlations of analogue 18a in mouse.**

Taking into account that the levels of serum RBP4 depend on formation of the RBP4-TTR-all-*trans*-retinol complex in circulation, we wanted to establish that a selective TTR tetramer binding ligand can allosterically antagonize the retinol-dependent RBP4-TTR interaction and potentially be capable of reducing circulating RBP4 levels *in vivo*. We evaluated the effect of a single oral dose of **18a** on dynamics of serum RBP4 levels in mice (Figure 6). After a single 25 mg/kg oral dose of **18a**, a maximal 66% reduction in serum RBP4 levels was observed 2 h following the dose administration (Figure 6, A). Oral administration of **18a** induced no changes in serum TTR levels (data not shown). The dynamics of serum RBP4 changes induced by **18a** demonstrated a very good correlation between the presence of the compound in circulation after oral dosing (Figure 6, B) and a reduction in serum RBP4 (Figure 6, A). The maximal RBP4 reduction seen at the 1 and 2 h timepoints (Figure 6, A) correlated very well with rapid oral absorption (Table 6) that led to the high concentration of **18a** in the blood at timepoints of the maximal serum RBP4 reduction (Figure 6, B). Compound clearance by 24 h matches well with the lack of the PD response at this timepoint. It is unclear at this time how **18a** is allosterically inhibiting RBP4-TTR-all-*trans*-retinol complex formation, and future studies

will be conducted to help gain a better understanding of these observations. In general, this data proves that there is a very good PK-PD relationship between **18a** exposure and serum RBP4 lowering activity in mice. In our previous work we proved a direct correlation between serum RBP4 lowering induced by different classes of selective RBP4 antagonists and bisretinoid-lowering efficacy in the *Abca4*^{-/-} mouse model of Stargardt disease.[40, 45, 46] Based on the very good *in vivo* RBP4 lowering activity exhibited by **18a**, it is expected that this compound may be efficacious in suppressing the formation of cytotoxic lipofuscin bisretinoids in the retina, which justifies evaluation of selective TTR ligands as a class of potential therapeutics for the treatment of Stargardt disease, dry AMD and other conditions characterized by enhanced accumulation of lipofuscin in the retina.
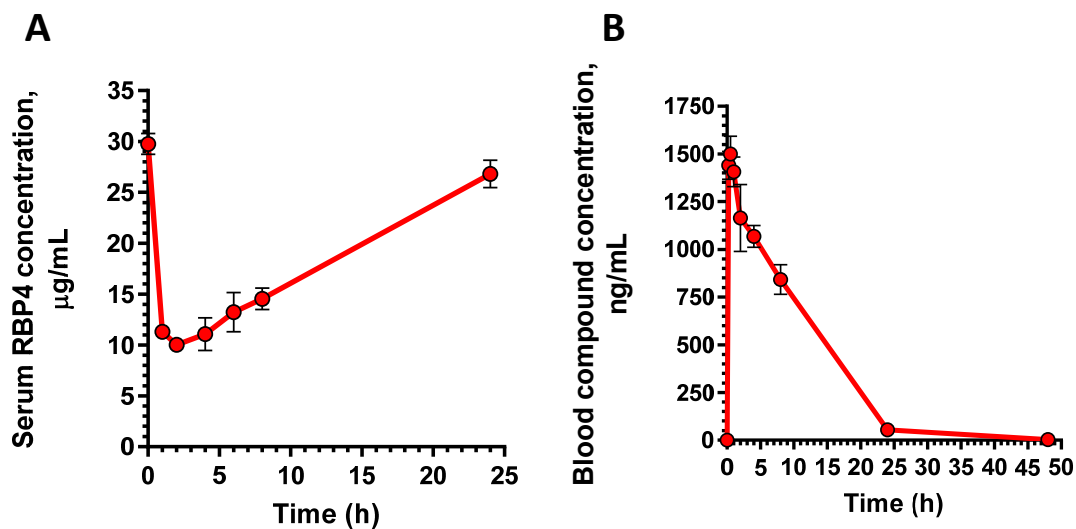

Figure 6. Pharmacokinetic and pharmacodynamic properties of 18a in mice. (A) Serum RBP4 levels following a single 25 mg/kg oral administration of **18a**. (B) Blood compound levels

following administration of a single oral 5 mg/kg dose of **18a**. Data are presented as means ± SD. Three mice per treatment group were used in the PK-PD study.

CONCLUSIONS

Inherited Stargardt disease and dry AMD are the forms of macular degeneration that may potentially be treated by pharmacological inhibition of lipofuscin bisretinoid synthesis in the retina. Only one class of compounds, competitive antagonists of retinol binding to RBP4, was currently known to block the all-*trans*-retinol-dependent RBP4-TTR interaction and reduce cytotoxic bisretinoid production in the animal models of excessive lipofuscin accumulation. However, the use of selective RBP4 antagonists may not be optimal in patients who, in addition to macular degeneration, may also be predisposed to genetic or sporadic forms of TTR amyloidosis. Holo-RBP4-TTR interaction stabilizes a portion of TTR tetramers circulating in a bloodstream thus preventing formation of TTR amyloid fibrils. Selective RBP4 antagonists release the TTR tetramer from the serum retinol-RBP4-TTR complex, and the release of a pool of unliganded TTR may be associated with destabilization of TTR tetramers. We hypothesized that ligands that selectively bind to TTR and not to RBP4 may also be capable of allosterically antagonizing all-*trans*-retinol-dependent RBP4-TTR tertiary complex formation. Such selective TTR ligands may induce a desired reduction in serum RBP4 levels required for inhibition of lipofuscin bisretinoid synthesis in the retina while providing adequate TTR tetramer kinetic stabilization. To our knowledge, prior to the work reported herein, TTR had not been considered as a drug target for mechanisms or indications that may be treated via RBP4 antagonists. In the reported work we sought to identify novel TTR

tetramer kinetic stabilizers that may also demonstrate robust RBP4 lowering capability *in vivo*. We utilized previously reported X-ray crystallographic data (PDB 4HIQ) and SAR for clinically investigated AG10 (**4**) to enable our structure-based drug design campaign. Our goal was to identify novel and conformationally constrained compounds that could provide favorable TTR tetramer kinetic stabilization, and we initially prepared a piperazine ring core linker congener (**18a**), which was found to exhibit excellent potency at TTR (FP IC$_{50}$ = 220 nM). Follow-up analogues of **18a** included a focused sample set containing alternately substituted benzoic acid appendages as well as analogues that explored SAR effects with alternative pyrazole head groups. Compound **18a** emerged as a lead upon conclusion of our SAR campaigns and was found to possess a desirable ADME profile and excellent PK characteristics in mouse. Analogue **18a** significantly decreases the formation of TTR high molecular weight aggregates in a manner comparable to tafamidis (**3**) in an *in vitro* TTR aggregation assay proving its activity as a TTR kinetic stabilizer. Furthermore, the compound induced a robust and sustained lowering (maximal 66% reduction) of serum RBP4 levels upon oral dosing in mice. As previously stated, it is currently unclear how **18a** is allosterically inhibiting RBP4-TTR-all-*trans*-retinol complex formation, and future studies will be conducted to help gain a better understanding of these observations. However, these data suggest that compound **18a** may be efficacious in suppressing the formation of cytotoxic lipofuscin bisretinoids in the retina while preventing possible TTR amyloid fibril formation. This justifies evaluation of selective TTR tetramer ligands as a class of potential therapeutics for Stargardt disease, dry AMD and other conditions characterized by enhanced

accumulation of lipofuscin in the retina, especially in patients who are also prone to ATTR comorbidities such as sporadic SSA or hereditary TTR amyloidosis.

EXPERIMENTAL SECTION

Fluorescence Polarization TTR Tetramer Binding Assay. Compound binding to TTR was assessed in the fluorescence polarization assay.[48] The assay measured competitive displacement of the fluorescent probe, FITC-diclofenac, from TTR isolated from human plasma (Clabiochem-Millipore, cat. No. 52957). FITC-diclofenac was synthesized at LeadGen Labr, LLC. Each well contained 200 nM TTR and 100 nM FITC-diclofenac in the FP buffer (10 mM Tris-HCl pH 7.5, 150 mM NaCl, 0.01% CHAPS, 0.01%Prionex) along with test compounds. Nonspecific binding was determined in the presence of 500 μM unlabeled diclofenac (Sigma-Aldrich). Reactions with test compounds were incubated overnight at 4 °C and FP was measured on SpectramaxM5e plate reader (Molecular Devices).

TTR Aggregation Assay. The ability of test compounds to prevent TTR aggregation was evaluated under the acidic conditions that favor TTR aggregation and fibril formation.[48] A 2 μl solution of 167 μM human TTR (ACRO Biosystems #H5223) was incubated with 7 μl 50 mM sodium acetate (pH = 4.0) (Sigma # S7545), 100 mM KCl (Sigma # S5405) in the presence or absence of 1 μl TTR inhibitor for 72 h at 37 °C. At the end of the incubation, 3.5 μl 500 mM sodium phosphate (Sigma #S5136) buffer (pH = 8.0) was added to each sample for neutralization and 0.6 μl 5% CHAPS (Sigma #C5070) as a detergent to prevent reassociation of protein. The cross-linking was performed by adding 1.5 μl 5% glutaraldehyde solution (Sigma# G6257). After 4 min, the reaction was

stopped by the addition of 2.5 µl freshly made 5% NaBH$_4$. Samples were subjected to

TTR western blotting with prealbumin antibodies (1:500; Dako #A0002). Band intensity

for TTR monomer and TTR aggregates was quantified from scanned images of the blots.

In vitro **binding of compounds to RBP4.** Compound binding to RBP4 was assessed in

the radiometric scintillation proximity (SPA) assay that was previously described.[41, 42, 48]

The assay measured competitive displacement of radiolabeled [^{3}H]-all-*trans*-retinol

from native RBP4 purified from human urine (Fitzgerald, 30R-AR022L). The protein was

biotinylated using the EZ-link Sulfo-NHS-LC-Biotinylation kit from ThermoFisher (Cat

#21335) as recommended by the manufacturer. Binding assays were implemented in a

final volume of 100 µL in SPA buffer (1 × PBR, pH 7.4, 1 mM EDTA, 0.1% BRA, 0.5%

CHAPS). The assay reaction included a radioligand, 10 nM [^{3}H]-all-*trans*-retinol (48.7

Ci/mmol; PerkinElmer, Waltham, MA), along with the 0.3 mg/well Streptavidin-PVT

beads (PerkinElmer, RPNQ0006) and 50 nM biotinylated human RBP4. Unlabeled retinol

(Sigma, cat # 95144) at 20 µM was added to control wells to assess a nonspecific

binding. Radioactivity counts were measured using CHAMELEON plate reader (Hidex Oy,

Turku, Finland) after 16 h of incubation at rt with mild shaking.

General Chemistry. All reactions were performed under a dry atmosphere of

nitrogen unless otherwise specified. Indicated reaction temperatures refer to the

reaction bath, while room temperature (rt) is noted as 25 °C. Commercial grade

reagents and anhydrous solvents were used as received from vendors and no attempts

were made to purify or dry these components further. Removal of solvents under

reduced pressure was accomplished with a Buchi rotary evaporator at approximately 28

mm Hg pressure using a Teflon-linked KNF vacuum pump. The measurement of pH for neutralizations or acidifications was measured with Hydrion pH paper (MicroEssential Lab). Thin layer chromatography was performed using 1" x 3" AnalTech No. 02521 silica gel plates with fluorescent indicator. Visualization of TLC plates was made by observation with either short wave UV light (254 nm lamp), 10% phosphomolybdic acid in ethanol or in iodine vapors. Preparative thin layer chromatography was performed using Analtech, 20 × 20 cm, 1000 micron preparative TLC plates. Flash column chromatography was carried out using a Teledyne Isco CombiFlash Companion Unit and a Biotage® Selekt System with Teledyne Isco RediSep Rf and Biotage Sfär silica gel columns. If needed, products were purified by reverse phase chromatography, using a Teledyne Isco CombiFlash Companion Unit and a Biotage® Selekt System with a RediSep Gold C18 reverse phase column. Proton NMR spectra were obtained on a 400 MHz Varian nuclear magnetic resonance spectrometer. Chemical shifts (δ) are reported in parts per million (ppm) and coupling constant (J) values are given in Hz, with the following spectral pattern designations: s, singlet; d, doublet; t, triplet, q, quartet; quint, quintet; m, multiplet; dd, doublet of doublets; dt, doublet of triplets; dq; doublet of quartets; br, broad signal. Tetramethylsilane was used as an internal reference. Peak listing, multiplicity designations, and coupling constant calculations were conducted using Mnova v.14 software (Mestrelab Research). Carbon NMR spectra were obtained on a 500 MHz Bruker AV III nuclear magnetic resonance spectrometer and tetramethylsilane was used as an internal reference. Fluorine NMR spectra were obtained on a 400 MHz Bruker AV III nuclear magnetic resonance spectrometer. Any

46

melting points provided are uncorrected and were obtained using a Stanford Research Systems OptiMelt melting point apparatus (MPA100) with an automated melting point system. Mass spectroscopic analyses were performed using ESI ionization on a Waters AQUITY UPLC MS triple quadrapole mass spectrometer. High pressure liquid chromatography (HPLC) purity analysis was performed using a Waters Breeze2 HPLC system with a binary solvent system A and B using a gradient elusion [A, H_2O with 0.1% formic acid; B, CH_3CN with 0.1% formic acid] and flow rate = 0.5 mL/min, with UV detection at 254 nm (system equipped with a photodiode array (PDA) detector). An ACQUITY UPLC BEH C18 column, 130 Å, 1.7 µm, 2.1 mm × 50 mm was used. High resolution mass spectrometry (HRMS) analysis was was performed using an Agilent 6530 Accurate-Mass Q-TOF. All final compounds tested for *in vitro* and *in vivo* biological testing were purified to ≥95% purity, and these purity levels were measured by both ^{1}H NMR and HPLC.

*3-(4-(3,5-Dimethyl-1H-pyrazol-4-yl)piperazin-1-yl)-4-fluorobenzoic Acid (**18a**).* Step A: A mixture of *tert*-butyl piperazine-1-carboxylate (**13**, 2.00 g, 10.7 mmol) and methyl 3-bromo-4-fluorobenzoate (2.25 g, 9.67 mmol) in anhydrous 1,4-dioxane (50 mL) was degassed with N_2 for 5 min. Cs_2CO_3 (10.0 g, 32.2 mmol), X-Phos (0.600 g, 1.29 mmol) and $Pd_2(dba)_3$ (0.491 g, 0.53 mmol) were then added and the mixture was stirred reflux for 16 h under an atmosphere of N_2. The mixture was allowed to cool to rt and then concentrated under reduced pressure. The resulting residue was chromatographed over silica gel (0-30% EtOAc in hexanes) to give *tert*-butyl 4-(2-fluoro-5-

(methoxycarbonyl)phenyl)piperazine-1-carboxylate (**14a**) as a brown oil (3.0 g, 83%). The material was used as is in the next step: ESI MS m/z 339 [M + H]⁺.

Step B: To a 0 °C cooled solution of *tert*-butyl 4-(2-fluoro-5-(methoxycarbonyl)phenyl)piperazine-1-carboxylate (**14a**, 3.00 g, 8.87 mmol) in CH_2Cl_2 (30 mL) was added TFA (6.7 mL, 88.7 mmol) and the resulting solution was stirred at rt for 16 h while gradually warming to rt. The mixture was then concentrated under reduced pressure and diluted with H_2O (30 mL), basified with saturated aqueous $NaHCO_3$ solution (50 mL), and extracted with EtOAc (3 × 50 mL). The combined organic extracts were washed with brine (50 mL), dried over Na_2SO_4, filtered, and concentrated under reduced pressure. The crude material was triturated with Et_2O and filtered to give pure methyl 4-fluoro-3-(piperazin-1-yl)benzoate (**15a**) as a white solid (1.20 g, 60%): ¹H NMR (400 MHz, CDCl₃) δ 9.85 (br, 1H), 7.72-7.69 (m, 1H), 7.63-7.60 (m, 1H), 7.21-7.04 (m, 1H), 3.87 (s, 3H), 3.35 (s, 8H); ESI MS *m/z* 239 [M + H]⁺.

Step C: To a 0 °C cooled solution of methyl 4-fluoro-3-(piperazin-1-yl)benzoate (**15a**, 1.20 g, 5.02 mmol) in anhydrous DMF (10 mL) were added *i*-Pr₂NEt (0.9 mL, 5.02 mmol) and 3-chloropentane-2,4-dione (0.672 g, 5.02 mmol) simultaneously and the resulting solution was stirred for 16 h under N_2 atmosphere while gradually warming to rt. The mixture was then diluted with H_2O (50 mL) and extracted with EtOAc (3 × 50 mL). The combined organic extracts were washed with brine, dried over Na_2SO_4, and concentrated under reduced pressure. The resulting residue was chromatographed over silica gel (0-50% EtOAc in hexanes) to give methyl 3-(4-(2,4-dioxopentan-3-yl)piperazin-1-yl)-4-fluorobenzoate (**16a**) as a brown oil (0.600 g, 35%): ¹H NMR (400 MHz, CDCl₃)

δ 7.64-7.62 (m, 2H), 7.06-7.01 (m, 1H), 3.86 (s, 1H), 3.31-3.09 (m, 4H), 3.09-3.05 (m, 4H), 2.27 (s, 1H), 2.24 (s, 6H); ESI MS m/z 337 [M + H]$^+$.

Step D: To a solution of methyl 3-(4-(2,4-dioxopentan-3-yl)piperazin-1-yl)-4-fluorobenzoate (**16a**, 0.500 g, 1.48 mmol) in CH_3OH (10 mL) was added $N_2H_2 \cdot H_2O$ (0.2 mL, 2.67 mmol, 64-65% solution in H_2O) and the resulting mixture stirred at rt for 1 h. The mixture was then concentrated under reduced pressure and the resulting residue was chromatographed over silica gel (0-50% EtOAc in hexanes) to give methyl 3-(4-(3,5-dimethyl-1*H*-pyrazol-4-yl)piperazin-1-yl)-4-fluorobenzoate (**17a**) as a brown solid (0.420 g, 85%): ^{1}H NMR (400 MHz, CDCl$_3$) δ 7.67-7.63 (m, 2H), 7.04-7.01 (m, 1H), 3.86 (s, 1H), 3.16-3.15 (m, 4H), 3.15-3.11 (m, 4H), 2.24 (s, 6H); ESI MS m/z 333 [M + H]$^+$.

Step E: To a solution of methyl 3-(4-(3,5-dimethyl-1*H*-pyrazol-4-yl)piperazin-1-yl)-4-fluorobenzoate (**17a**, 0.420 g, 1.26 mmol) in CH_3OH (4 mL), THF (4 mL) and H_2O (2 mL) was added LiOH (91 mg, 3.79 mmol). The reaction mixture was stirred at rt for 16 h and was concentrated under reduced pressure. The aqueous layer was then diluted with H_2O (30 mL) and neutralized to approximately pH = 7 with 2 N aqueous HCl (monitored with Hydrion pH paper). The aqueous mixture was extracted with EtOAc (3 × 50 mL) and the combined organic solution was washed with brine, dried over Na_2SO_4, and concentrated under reduced pressure. The crude residue was chromatographed over silica gel (0-10% CH_3OH in CH_2Cl_2) to give 3-(4-(3,5-dimethyl-1*H*-pyrazol-4-yl)piperazin-1-yl)-4-fluorobenzoic acid (**18a**) as a white solid (0.390 g, 97%): melting point = 220 - 222 °C; ^{1}H NMR (400 MHz, DMSO-d_6) δ 7.53-7.55 (m, 2H, H$_1$ and H$_2$), 7.23-7.18 (dt, J = 12 Hz, 3.2 Hz, 1H, H$_3$), 3.04 (m, 4H, H$_4$), 3.01 (m, 4H, H$_5$), 2.10 (s, 6H, H$_6$); ^{13}C NMR (500 MHz,

DMSO-d_6) δ 128.7, 121.7, 124.1, 124.0, 120.2, 120.2, 116.3, 116.2; ^{19}F NMR (400 MHz, DMSO-d_6) δ -116.0 (s, F); ESI MS *m/z* 319 [M + H]$^+$; HRMS (ESI$^+$) $C_{16}H_{19}FN_4O_2$ calcd [M + H]$^+$ = 319.157, observed [M + H]$^+$ = 319.1562; combustion analysis (%CHN): calcd for $C_{16}H_{19}FN_4O_2$ · 0.5 H_2O · 0.5 HCl: %C = 55.61; %H = 5.98; %N = 16.21; found: %C = 55.88; %H = 5.74; %N = 15.97; HPLC >99% (AUC), t_R = 11.5 min.

*3-(4-(3,5-Dimethyl-1H-pyrazol-4-yl)piperazin-1-yl)benzoic Acid (**18b**).* Compound **18b** was prepared from *tert*-butyl piperazine-1-carboxylate (**13**) and methyl 3-bromobenzoate according to a similar procedure described for the synthesis of **18a**: ^{1}H NMR (400 MHz, DMSO-d_6) δ 7.48 (s, 1H), 7.36 (m, 2H), 7.23 (m, 1H), 3.23 (m, 4H), 3.04 (m, 4H), 2.14 (s, 6H); ESI MS *m/z* 301[M + H]$^+$; HPLC >99% (AUC), t_R = 10.7 min.

*3-(4-(3,5-Dimethyl-1H-pyrazol-4-yl)piperazin-1-yl)-4-methoxybenzoic Acid (**18c**).* Compound **18c** was prepared from *tert*-butyl piperazine-1-carboxylate (**13**) and methyl 3-bromo-4-methoxybenzoate according to a similar procedure described for the synthesis of **18a**: ^{1}H NMR (400 MHz, DMSO-d_6) δ 7.58 (dd, *J* = 8.4 Hz, 2.0 Hz, 1H), 7.44 (d, *J* = 2.0 Hz, 1H), 7.01 (d, *J* = 8.4 Hz, 1H), 3.83 (s, 3H), 2.99 (s, 8H), 2.08 (s, 6H); ESI MS *m/z* 331 [M + H]$^+$; HPLC 94.6 % (AUC), t_R = 10.2 min.

*3-(4-(3,5-Dimethyl-1H-pyrazol-4-yl)piperazin-1-yl)-4-methylbenzoic Acid (**18d**).* Compound **18d** was prepared from *tert*-butyl piperazine-1-carboxylate (**13**) and methyl 3-bromo-4-methylbenzoate according to a similar procedure described for the synthesis of **18a**: ^{1}H NMR (400 MHz, DMSO-d_6) δ 7.57 (d, *J* = 1.2 Hz, 1H), 7.53 (d, *J* = 8.0 Hz, 1H), 7.27 (d, *J* = 8.0 Hz, 1H), 3.01 (m, 4H), 2.90 (m, 4H), 2.46 (s, 3H), 2.12 (s, 6H); ESI MS *m/z* 315 [M + H]$^+$; HPLC >99% (AUC), t_R = 11.2 min.

3-(4-(3,5-Dimethyl-1H-pyrazol-4-yl)piperazin-1-yl)-4-(trifluoromethyl)benzoic   Acid (18e). Compound **18e** was prepared from *tert*-butyl piperazine-1-carboxylate (**13**) and methyl 3-bromo-4-(trifluoromethyl)benzoate according to a similar procedure described for the synthesis of **18a**: ^{1}H NMR (400 MHz, DMSO-d_6) δ 7.99 (s, 1H), 7.84 (d, *J* = 8.4 Hz, 1H), 7.78 (d, *J* = 8.4 Hz, 1H), 2.97 (m, 4H), 2.94 (m, 4H), 2.11 (s, 6H); ESI MS *m/z* 369 [M + H]$^+$; HPLC 98.7% (AUC), t_R = 11.9 min.

4-Chloro-3-(4-(3,5-dimethyl-1H-pyrazol-4-yl)piperazin-1-yl)benzoic   Acid   (18f). Compound **18f** was prepared from *tert*-butyl piperazine-1-carboxylate (**13**) and methyl 3-bromo-4-chlorobenzoate according to a similar procedure described for the synthesis of **18a**: ^{1}H NMR (400 MHz, DMSO-d_6) δ 7.66 (s, 1H), 7.58 (d, *J* = 8.4 Hz, 1H), 7.51 (d, *J* = 10.8 Hz, 1H), 3.04 (br, 8H), 2.12 (s, 6H); ESI MS *m/z* 335 [M + H]$^+$; HPLC 98.0% (AUC), t_R = 11.5 min.

3-(4-(3,5-Dimethyl-1H-pyrazol-4-yl)piperazin-1-yl)-2-fluorobenzoic   Acid   (18g). Compound **18g** was prepared from *tert*-butyl piperazine-1-carboxylate (**13**) and methyl 3-bromo-2-fluorobenzoate according to a similar procedure described for the synthesis of **18a**: ^{1}H NMR (400 MHz, DMSO-d_6) δ 7.29 (m, 1H), 7.19 (m, 1H), 7.12 (t, *J* = 9.6 Hz, 1H), 3.03 (br, 8H), 2.12 (s, 6H); ESI MS *m/z* 319 [M + H]$^+$; HPLC 98.3% (AUC), t_R = 10.3 min.

5-(4-(3,5-Dimethyl-1H-pyrazol-4-yl)piperazin-1-yl)-2-fluorobenzoic   Acid   (18h). Compound **18h** was prepared from *tert*-butyl piperazine-1-carboxylate (**13**) and methyl 5-bromo-2-fluorobenzoate according to a similar procedure described for the synthesis of **18a**: ^{1}H NMR (400 MHz, DMSO-d_6) δ 7.29 (m, 1H), 7.19 (m, 1H), 7.12 (t, *J* = 9.6 Hz, 1H),

3.13 (br, 4H), 2.99 (br, 4H), 2.10 (s, 6H); ESI MS *m/z* 319 [M + H]⁺; HPLC >99% (AUC), t_R = 10.6 min.

3-(4-(3,5-Dimethyl-1H-pyrazol-4-yl)piperazin-1-yl)-5-fluorobenzoic *Acid* *(18i).* Compound **18i** was prepared from *tert*-butyl piperazine-1-carboxylate (**13**) and methyl 3-bromo-5-fluorobenzoate according to a similar procedure described for the synthesis of **18a**: ¹H NMR (400 MHz, DMSO-*d₆*) δ 7.28 (s, 1H), 6.99 (m, 2H), 3.24 (m, 4H), 2,98 (m, 4H), 2.10 (s, 6H); ESI MS *m/z* 319 [M + H]⁺; HPLC 97.6% (AUC), t_R = 11.3 min.

5-(4-(3,5-Dimethyl-1H-pyrazol-4-yl)piperazin-1-yl)-4-fluoro-2-methylbenzoic *Acid* *(18j).* Compound **18j** was prepared from *tert*-butyl piperazine-1-carboxylate (**13**) and methyl 5-bromo-4-fluoro-2-methylbenzoate according to a similar procedure described for the synthesis of **18a**: ¹H NMR (400 MHz, DMSO-*d₆*) δ 7.52 (d, *J* = 8.4 Hz, 1H), 7.13 (d, *J* = 13.2 Hz, 1H), 3.04 (br, 8H), 2.45 (s, 1H), 2.13 (s, 6H); ESI MS *m/z* 333 [M + H]⁺; HPLC 98.7% (AUC), t_R = 11.6 min.

3-((3aR,6aS)-5-(3,5-Dimethyl-1H-pyrazol-4-yl)hexahydropyrrolo[3,4-c]pyrrol-2(1H)-yl)-4-fluorobenzoic Acid (19). Compound **19** was prepared from *tert*-butyl (3aR,6aS)-hexahydropyrrolo[3,4-c]pyrrole-2(1H)-carboxylate and methyl 3-bromo-4-fluorobenzoate according to a similar procedure described for the synthesis of **18a**: ¹H NMR (400 MHz, DMSO-*d₆*) δ 7.40 (m, 2H), 7.16 (m, 1H), 3.60 (m, 2H), 3.20 (m, 2H), 3.01 (m, 2H), 2.88 (m, 4H), 2.11 (s, 6H); ESI MS *m/z* 345 [M + H]⁺; HPLC 95.4% (AUC), t_R = 11.0 min.

(±)-3-(7-(3,5-Dimethyl-1H-pyrazol-4-yl)-2,7-diazaspiro[4.4]nonan-2-yl)-4-fluorobenzoic Acid (20). Compound **20** was prepared from *tert*-butyl 2,7-

diazaspiro[4.4]nonane-2-carboxylate and methyl 3-bromo-4-fluorobenzoate according to a similar procedure described for the synthesis of **18a**: ^{1}H NMR (400 MHz, DMSO-d_6) δ 7.25 (m, 2H), 7.14 (m, 1H), 3.46 (m, 4H), 3.02 (m, 2H), 2.99 (m, 2H), 2.11 (s, 6H), 1.94-1.87 (m, 4); ESI MS m/z 359 [M + H]$^+$; HPLC 97.3% (AUC), t_R = 11.3 min.

3-(6-(3,5-Dimethyl-1H-pyrazol-4-yl)-2,6-diazaspiro[3.3]heptan-2-yl)-4-fluorobenzoic Acid (21). Compound **21** was prepared from *tert*-butyl 2,6-diazaspiro[3.3]heptane-2-carboxylate and methyl 3-bromo-4-fluorobenzoate according to a similar procedure described for the synthesis of **18a**: ^{1}H NMR (400 MHz, DMSO-d_6) δ 7.31 (m, 1H), 7.17 (t, *J* = 9.2 Hz, 1H), 7.7 (d, *J* = 8.4 Hz, 1H), 4.09 (m, 4H), 3.96 (m, 4H), 2.10 (s, 6H); ESI MS m/z 331 [M + H]$^+$; HPLC 98.8% (AUC), t_R = 10.7 min.

3-(4-(3,5-Dimethylisoxazol-4-yl)piperazin-1-yl)-4-fluorobenzoic Acid (23). Step A: To a solution of methyl 3-(4-(2,4-dioxopentan-3-yl)piperazin-1-yl)-4-fluorobenzoate (**16a**, 80.0 mg, 0.23 mmol) in CH$_3$OH (2 mL) was added NH$_2$OH·HCl (32.0 mg, 0.47 mmol) and the resulting solution was stirred at rt for 16 h. The mixture was concentrated under reduced pressure and the resulting residue was chromatographed over silica gel (0-50% EtOAc in hexanes) to give methyl 3-(4-(3,5-dimethylisoxazol-4-yl)piperazin-1-yl)-4-fluorobenzoate (**22**) as a brown solid (20.1 mg, 25%); ESI MS *m/z* 334 [M + H]$^+$.

Step B: To a solution of methyl 3-(4-(3,5-dimethylisoxazol-4-yl)piperazin-1-yl)-4-fluorobenzoate (**22**, 8.1 mg, 0.023 mmol) in CH$_3$OH (1 mL), THF (1 mL) and H$_2$O (0.5 mL) was added LiOH (2.7 mg, 0.11 mmol). The reaction mixture was stirred at rt for 16 h and then concentrated under reduced pressure. The aqueous layer was diluted with H$_2$O (15 mL) and neutralized with 2 N aqueous HCl. The aqueous mixture was extracted with

EtOAc (3 × 10 mL) and the combined organic extracts were washed with brine, dried over Na_2SO_4, filtered, and concentrated under reduced pressure. The resulting residue was chromatographed over silica gel (0-10% CH_3OH in CH_2Cl_2) to give 3-(4-(3,5-dimethylisoxazol-4-yl)piperazin-1-yl)-4-fluorobenzoic acid (**23**) as a white solid (2.5 mg, 34%): ^{1}H NMR (400 MHz, DMSO-d_6) δ 7.71-7.59 (m, 1H), 7.19-7.10 (m, 2H), 3.18-3.3.17 (m, 4H), 3.12-3.11 (m, 4H), 2.38 (s, 3H), 2.25 (s, 3H); ESI MS *m/z* 320 [M + H][+]; HPLC 96.8% (AUC), t_R = 13.7 min.

*3-(4-(2H-Tetrazol-5-yl)piperazin-1-yl)-4-fluorobenzoic Acid (**25**).* Step A: To a 0 °C cooled solution of methyl 4-fluoro-3-(piperazin-1-yl)benzoate (**15a**, 0.200 g, 0.84 mmol) and *i*-Pr$_2$NEt (0.5 mL, 2.52 mmol) in THF (3 mL) was added CNBr (0.106 g, 1.01 mmol), and the mixture stirred for 1 h while gradually warming to rt. The mixture was concentrated under reduced pressure and the residue was dissolved in DMF (3 mL). To this solution was added NH_4Cl (0.449 g, 8.4 mmol) and NaN_3 (0.546 g, 8.4 mmol) and the resulting mixture heated at 120 °C for 12 h. The mixture was then allowed to cooled to rt, diluted with H_2O (10 mL), and was extracted with EtOAc (3 × 50 mL). The combined organic extracts were washed with brine, dried over Na_2SO_4, filtered, and concentrated under reduced pressure to give methyl 3-(4-(2*H*-tetrazol-5-yl)piperazin-1-yl)-4-fluorobenzoate (0.160 g), which was taken into next step as is without purification: ESI MS *m/z* 307 [M + H][+].

Step B: To a solution of methyl 3-(4-(2*H*-tetrazol-5-yl)piperazin-1-yl)-4-fluorobenzoate (0.160 g, 0.52 mmol) in CH_3OH (4 mL), THF (4 mL) and H_2O (2 mL) was added LiOH (0.125 g, 5.2 mmol) and the resulting mixture stirred at rt for 16 h. The

mixture was then concentrated under reduced pressure and the aqueous layer was diluted with H_2O (15 mL) and acidified to pH = 3 with 2 N aqueous HCl. The aqueous mixture was then extracted with EtOAc (3 × 10 mL) and the combined organic extracts were washed with brine, dried over Na_2SO_4, filtered, and concentrated under reduced pressure. The resulting residue was chromatographed over silica gel (0-10% CH_3OH in CH_2Cl_2) to give 3-(4-(2*H*-tetrazol-5-yl)piperazin-1-yl)-4-fluorobenzoic acid (**25**) as a white solid (80.2 mg, 53%): ^{1}H NMR (400 MHz, DMSO-*d*$_6$) δ 7.59 (m, 2H), 7.25 (dd, *J* = 7.6 Hz, *J* = 3.6 Hz, 1H), 3.52 (br, 4H), 3.14 (br, 4H); ESI MS *m/z* 293 [M + H]$^+$; HPLC 98.3% (AUC), *t*$_R$ = 11.3 min.

*4-Fluoro-3-(4-(2-(trifluoromethyl)phenyl)piperazin-1-yl)benzoic Acid (**27**).* Step A: A mixture of methyl 4-fluoro-3-(piperazin-1-yl)benzoate (**15a**, 0.200 g, 0.84 mmol) and 1-bromo-2-(trifluoromethyl)benzene (0.226 g, 1.17 mmol) in anhydrous 1,4-dioxane (10 mL) was degassed with N_2 for 5 min. Cs_2CO_3 (0.816 g, 2.50 mmol), X-Phos (79.1 mg, 0.16 mmol) and $Pd_2(dba)_3$ (76.0 mg, 0.08 mmol) were then added and the reaction mixture was stirred at reflux for 16 h under an atmosphere of N_2. The mixture was allowed to cool to rt and concentrated under reduced pressure. The resulting residue was chromatographed over silica gel (0-30% EtOAc in hexanes) to give methyl 4-fluoro-3-(4-(2-(trifluoromethyl)phenyl)piperazin-1-yl)benzoate (**26**) (30.2 mg, 9%) as a brown solid: ^{1}H NMR (400 MHz, CDCl$_3$) δ 7.69-7.63 (m, 3H), 7.61-7.60 (m, 1H), 7.52-7.41 (m, 1H), 7.08-7.03 (m, 2H), 3.88 (m, 3H), 3.25-3.23 (m, 4H), 3.10-3.08 (m, 4H); ESI MS *m/z* 383 [M + H]$^+$.

Step B: To a solution of methyl 4-fluoro-3-(4-(2-(trifluoromethyl)phenyl)piperazin-1-yl)benzoate (**26**, 30.0 mg, 0.78 mmol) in CH_3OH (4 mL), THF (4 mL) and H_2O (2 mL) was added LiOH (9 mg, 0.39 mmol). The mixture was stirred at rt for 16 h and then concentrated under reduced pressure. The aqueous layer was diluted with H_2O (10 mL) and acidified to pH = 3 with 2 N aqueous HCl. The aqueous mixture was extracted with EtOAc (3 × 10 mL) and the combined organic extracts were washed with brine, dried over Na_2SO_4, filtered, and concentrated under reduced pressure. The resulting residue was chromatographed over silica gel (0-10% CH_3OH in CH_2Cl_2) to give 4-fluoro-3-(4-(2-(trifluoromethyl)phenyl)piperazin-1-yl)benzoic acid (**27**) as a white solid (15.2 mg, 49%): ^{1}H NMR (400 MHz, $CDCl_3$) δ 7.76-7.72 (m, 2H), 7.64 (d, J = 8.0 Hz, 1H), 7.52-7.50 (m, 1H), 7.42 (d, J = 8.0 Hz, 1H), 7.23 (m, 1H), 7. 10 (dd, J = 8.0 Hz, J = 4.0 Hz, 1H), 3.26 (m, 4H), 3.11 (m, 4H); ESI MS m/z 369 [M + H]$^+$; HPLC 96.7% (AUC), t_R = 16.0 min.

4-Fluoro-3-(4-((3-methyl-1H-pyrazol-5-yl)methyl)piperazin-1-yl)benzoic Acid (*29*). Step A: A solution of methyl 4-fluoro-3-(piperazin-1-yl)benzoate (**15a**, 0.200 g, 0.84 mmol) and 3-methyl-1*H*-pyrazole-5-carbaldehyde (0.111 g, 1.0 mmol) in 1,2-dichloroethane (5 mL), and HOAc (0.01 mL, 0.17 mmol) stirred at rt for 1 h. NaBH(OAc)$_3$ (0.267 g, 1.26 mmol) was then added and the mixture stirred for 12 h at 60 °C. The mixture was then allowed to cool to rt and diluted with CH_2Cl_2 (10 mL). The organic mixture was washed with saturated aqueous $NaHCO_3$ (10 mL), H_2O (10 mL) and brine. The organic layer was then dried over Na_2SO_4, filtered, and concentrated under reduced pressure. The resulting residue was chromatographed over silica gel (0-10% CH_3OH in

CH$_2$Cl$_2$) to give methyl 4-fluoro-3-(4-((3-methyl-1*H*-pyrazol-5-yl)methyl)piperazin-1-yl)benzoate (**28**) as a white solid (0.210 g, 76%): ESI MS *m/z* 333 [M + H]$^+$.

Step B: To a solution of methyl 4-fluoro-3-(4-((3-methyl-1*H*-pyrazol-5-yl)methyl)piperazin-1-yl)benzoate (**28**, 0.200 g, 0.60 mmol) in CH$_3$OH (4 mL), THF (4 mL) and H$_2$O (2 mL) was added LiOH (144.5 mg, 6.0 mmol) and the resulting mixture was stirred at rt for 16 h. The mixture was concentrated under reduced pressure and the resulting aqueous layer was diluted with H$_2$O (10 mL) and neutralized with 2 N aqueous HCl. The aqueous mixture was then extracted with EtOAc (13 × 10 mL) and the combined organic extracts were washed with brine, dried over Na$_2$SO$_4$, filtered, and concentrated under reduced pressure. The resulting residue was chromatographed over silica gel (0-10% CH$_3$OH in CH$_2$Cl$_2$) to give 4-fluoro-3-(4-((3-methyl-1*H*-pyrazol-5-yl)methyl)piperazin-1-yl)benzoic acid (**29**) as a white solid (0.120 g, 63%): ^{1}H NMR (400 MHz, DMSO-*d*$_6$) δ 7.50-7.46 (m, 2H), 7.33 (s, 1H), 7.13 (dd, *J* = 8.8 Hz, *J* = 4.0 Hz, 1H), 3.30 (s, 2H), 2.95 (br, 4H), 2.45 (br, 4H), 2.12 (s, 3H); ESI MS *m/z* 319 [M + H]$^+$; HPLC 98.7% (AUC), *t*$_R$ = 10.2 min.

*3-(4-(3,5-Dimethyl-1H-pyrazol-4-yl)piperazin-1-yl)-4-fluorobenzamide (**30**).* Step A: Step A: To a mixture of 3-(4-(3,5-dimethyl-1H-pyrazol-4-yl)piperazin-1-yl)-4-fluorobenzoic acid (**18a**, 0.100 g, 0.314 mmol), HBTU (0.178 g, 0.471 mmol), and *i*-Pr$_2$NEt (0.218 mL, 1.26 mmol) in DMF (4 mL) was added NH$_4$Cl (16.7 mg, 0.314 mmol). The resulting solution was stirred at rt for 18 h under an atmosphere of N$_2$. The mixture was diluted with H$_2$O (10 mL) and extracted with EtOAc (3 × 20 mL). The combined organic extracts were washed with H$_2$O (3 × 20 mL) and brine, dried over Na$_2$SO$_4$, filtered, and

concentrated under reduced pressure. The resulting crude residue was chromatographed over silica gel (0% to 80% EtOAc in hexanes) to give 3-(4-(3,5-dimethyl-1H-pyrazol-4-yl)piperazin-1-yl)-4-fluorobenzamide (**30**) as a white solid (71.7 mg, 72%): ^{1}H NMR (400 MHz, DMSO-d_6) δ 11.84 (br, 1H), 7.94 (bs, 1H), 7.54-7,48 (m, 2H), 7.31 (s, 1H), 7.14 (m, 1H), 3.06-3.01 (m, 8H), 2.10 (s, 6H); ESI MS m/z 318 [M + H][+]; HPLC >99% (AUC), t_R = 10.5 min.

1-(3,5-Dimethyl-1H-pyrazol-4-yl)-4-(2-fluoro-5-(2H-tetrazol-5-yl)phenyl)piperazine

(31). Step A: A mixture of 3-(4-(3,5-dimethyl-1H-pyrazol-4-yl)piperazin-1-yl)-4-fluorobenzamide (**30**, 0.180 g, 0.526 mmol), NaN$_3$ (0.142 g, 0.375 mmol), and tetrachlorosilane (98.5 mg, 0.579 mmol) in CH$_3$CN (4 mL) stirred at 80 °C for 18 h in a sealed vessel. The reaction mixture was allowed to cool to rt and diluted with saturated NaHCO$_3$ (5 mL). The aqueous mixture was extracted with CHCl$_3$ (3 × 50 mL) and the combined organic extracts were washed with brine (50 mL), dried over Na$_2$SO$_4$, filtered, and concentrated under reduced pressure. The resulting residue was chromatographed over silica gel (0% to 10% CH$_3$OH in CH$_2$Cl$_2$) to give 1-(3,5-dimethyl-1H-pyrazol-4-yl)-4-(2-fluoro-5-(2H-tetrazol-5-yl)phenyl)piperazine (**31**) as a white solid (60.3 mg, 30%): ^{1}H NMR (400 MHz, DMSO-d_6) δ 7.69 (m, 1H), 7.67 (m, 1H), 7.36-7. (dd, J = 4Hz, J = 8.4 Hz, 1H); 3.12 (m, 4H), 3.09 (m, 4H), 2.13 (s, 6H); ESI MS m/z 343 [M + H][+]; HPLC >99% (AUC), t_R = 11.1 min.

ASSOCIATED CONTENT

Supporting Information

The Supporting Information is available free of charge on the ACS publications website at http://pubr.acs.org.

The Supporting Information contains the following:

TTR *in vitro* assay protocols, TTR aggregation assay protocols, RBP4 *in vitro* assay protocols, mouse PK study protocols, serum RBP4 collection and measurement protocols, *in vitro* ADME assay protocols, general chemistry information, and spectroscopic and analytical data for compound **18a** (^{1}H NMR, ^{13}C NMR, ^{19}F NMR, MS, HRMS, and HPLC), molecular formula strings for biologically tested compounds (PDF);

Molecular formula strings for biologically tested compounds (CSV) is also provided.

AUTHOR INFORMATION

Corresponding Authors

Christopher L. Cioffi – Departments of Basic and Clinical Sciences and Pharmaceutical Sciences, Albany College of Pharmacy and Health Sciences, Albany, New York 12208, United States; orcid.org/0000-0003-0642-7905; Phone: 518-694- 7224; Email: christopher.cioffi@acphs.edu

Konstantin Petrukhin – Department of Ophthalmology, Columbia University Medical Center, New York, New York 10032, United States; orcid.org/0000-0002-5545-6924; Phone: 212-305-9040; Email: kep4@cumc.columbia.edu

Authors

Arun Raja – Departments of Basic and Clinical Sciences and Pharmaceutical Sciences, Albany College of Pharmacy and Health Sciences, Albany, New York 12208, United States

Parthasarathy Muthuraman – Departments of Basic and Clinical Sciences and Pharmaceutical Sciences, Albany College of Pharmacy and Health Sciences, Albany, New York 12208, United States

Aravindan Jayaraman – Departments of Basic and Clinical Sciences and Pharmaceutical Sciences, Albany College of Pharmacy and Health Sciences, Albany, New York 12208, United States

Srinivasan Jayakumar – Departments of Basic and Clinical Sciences and Pharmaceutical Sciences, Albany College of Pharmacy and Health Sciences, Albany, New York 12208, United States

Andras Varadi – Department of Ophthalmology, Columbia University Medical Center, New York, New York 10032, United States

Boglarka Racz – Department of Ophthalmology, Columbia University Medical Center, New York, New York 10032, United States

Complete contact information is available at:

this paper that are assigned to The Trustees of Columbia University in the City of New York and Albany College of Pharmacy and Health Sciences.

ACKNOWLEDGEMENTS

ABBREVIATIONS

$A\beta$, β-amyloid; *Abca4*, ATP-binding cassette, sub-family A (ABC), member 4; ADME, Absorption, Distribution, Metabolism, Elimination; AMD, age-related macular degeneration; aq, aqueous; Arg, arginine; ATTR, transthyretin amyloidosis; ATTR-CM, transthyretin amyloidosis cardiomyopathy; ATTR-PN, transthyretin amyloidosis polyneuropathy; AUC, area under the curve; Boc_2O, di-*tert*-butyl di-carbonate; CH_2Cl_2,

dichloromethane; CH$_3$CN, acetonitrile; CH$_3$OH, methyl alcohol; CL, clearance; CL$_{int}$, intrinsic clearance; Cs$_2$CO$_3$, cesium carbonate; CF$_3$, trifluoromethyl; CSF, cerebral spinal fluid; CYP, cytochrome P450; CYP2C9, cytochrome P450 2C9; CYP2C19, cytochrome P450 2C19; CYP2D6, cytochrome P450 2D6; CYP3A4, cytochrome P450 3A4; DMF; *N,N*-dimethylformamide; Et$_2$O, diethyl ether; EtOAc, ethyl acetate; %F, % oral bioavailability; FAC, familial amyloid cardiomyopathy; FAP, familial amyloid neuropathy; FITC, fluorescein isothiocyanate; FP, fluorescence polarization; Gln, glutamine; Glu, glutamic acid; Gly, glycine; h, hour(s); HBP, halogen binding pocket; HBTU, (2-(1H-benzotriazol-1-yl)-1,1,3,3-tetramethyluronium hexafluorophosphate; HCl, hydrochloric acid; hERG; human ether-a-go-go channel; HLM, human liver microsomes; HOAc, acetic acid;; HRMS, high resolution mass spectrometry; *i*-Pr$_2$NEt, *N,N*-diisopropylethylamine; IV, intravenous; LiOH, lithium hydroxide; Leu, leucine; Lys, lysine; min, minutes; MLM, mouse liver microsomes; NaBH$_4$, sodium borohydride; NaBH(OAc)$_3$, sodium triacetoxyborohydride; NaN$_3$, sodium azide; NH$_4$Cl, ammonium chloride; PBS, phosphate buffered saline; PD, pharmacodynamics; PDB, Protein Data Bank; Pd$_2$(dba)$_3$, tris(dibenzylideneacetone)dipalladium(0); Phe, phenylalanine; PK, pharmacokinetics; PO, oral; PPARγ, nuclear peroxisome proliferator-activated receptor-gamma; %PPB, % plasma protein binding; RBP4, retinol binding protein-4; RLM, rat liver microsomes; RPE, retinal pigment epithelium; rt, room temperature; SAR, structure-activity relationship; Ser, serine; SPA, scintillation proximity assay; SSA, systemic senile amyloidosis; TBG: thyroxine-binding globulin; TFA, trifluoroacetic acid; THF, tetrahydrofuran; Thr, threonine; TTR, transthyretin; Tyr, tyrosine; T4, thyroxine; Val, valine; V$_{ss}$, volume of

distribution at steady state; XPhos, 2-dicyclohexylphosphino-2',4',6'-triisopropylbiphenyl.

REFERENCES

1.   Vieira, M.; Saraiva, M. J. Transthyretin: a multifaceted protein. *Biomol. Concepts* **2014**, *5*, 45-54.

2.   Kassem, N. A.; Deane, R.; Segal, M. B.; Preston, J. E. Role of transthyretin in thyroxine transfer from cerebrospinal fluid to brain and choroid plexus. *Am. J. Physiol. Regul. Integr. Comp. Physiol.* **2006**, *291*, R1310-R1315.

3.   Gimeno, A.; Santos, L. M.; Alemi, M.; Rivas, J.; Blasi, D.; Cotrina, E. Y.; Llop, J.; Valencia, G.; Cardoso, I.; Quintana, J.; Arsequell, G.; Jimenez-Barbero, J. Insights on the interaction between transthyretin and Aβ in solution. A saturation transfer difference (STD) NMR analysis of the role of iododiflunisal. *J. Med. Chem.* **2017**, *60*, 5749-5758.

4.   Giao, T.; Saavedra, J.; Cotrina, E.; Quintana, J.; Llop, J.; Arsequell, G.; Cardoso, I., Undiscovered roles for transthyretin: from a transporter protein to a new therapeutic target for Alzheimer's disease. *Int. J. Mol. Sci.* **2020**, *21*, 2075.

5.   Gales, L.; Macedo-Ribeiro, S.; Arsequell, G.; Valencia, G.; Saraiva, M. J.; Damas, A. M. Human transthyretin in complex with iododiflunisal: structural features associated with a potent amyloid inhibitor. *Biochem. J.* **2005**, *388*, 615-621.

6.   Kanai, M.; Raz, A.; Goodman, D. S. Retinol-binding protein: the transport protein for vitamin A in human plasma. *J. Clin. Invest.* **1968,** *47*, 2025-2044.

7.   Hyung, S-J.; Deroo, S.; Robinson, C. V. Retinol and retinol-binding protein stabilize transthyretin via formation of retinol transport complex. *ACS. Chem. Biol.* **2010**, *5*, 1137-1146.

8.   Kawaguchi, R.; Zhong, M.; Kassai, M.; Ter-Stepanian, M.; Sun, H. Vitamin A transport mechanism of the multitransmembrane cell-surface receptor STRA6. *Membranes (Basel)* **2015**, *5*, 425-453.

9.   Sun, X.; Dyson, H. J.; Wright, P. E. Kinetic analysis of the multistep aggregation pathway of human transthyretin. *Proc. Natl. Acad. Sci. U S A* **2018**, *115*, E6201-E6208.

10.   Ruberg, F. L.; Grogan, M.; Hanna, M.; Kelly, J. W.; Maurer, M. S., Transthyretin amyloid cardiomyopathy: JACC state-of-the-art review. *J. Am. Coll. Cardiol.* **2019**, *73*, 2872-2891.

11.   Yamamoto, H.; Yokochi, T. Transthyretin cardiac amyloidosis: an update on diagnosis and treatment. *ESC Heart Fail.* **2019**, *6*, 1128-1139.

12.   Waddington-Cruz, M.; Schmidt, H.; Botteman, M. F.; Carter, J. A.; Stewart, M.; Hopps, M.; Fallet, S.; Amass, L. Epidemiological and clinical characteristics of

symptomatic hereditary transthyretin amyloid polyneuropathy: a global case series. *Orphanet. J. Rare Dis.* **2019**, *14*, 34.

13.   Park, G. Y.; Jamerlan, A.; Shim, K. H.; An, S. S. A. Diagnostic and treatment approaches involving transthyretin in amyloidogenic diseases. *Int. J. Mol. Sci.* **2019**, *20*, 2982.

14.   Leach, B. I.; Zhang, X.; Kelly, J. W.; Dyson, H. J.; Wright, P. E. NMR measurements reveal the structural basis of transthyretin destabilization by pathogenic mutations. *Biochemistry* **2018**, *57*, 4421-4430.

15.   Jesus, C. S.; Almeida, Z. L.; Vaz, D. C.; Faria, T. Q.; Brito, R. M. A new folding kinetic mechanism for human transthyretin and the influence of the amyloidogenic V30M Mutation. *Int. J. Mol. Sci.* **2016,** *17*, 1428.

16.   Damrauer, S. M.; Chaudhary, K.; Cho, J. H.; Liang, L. W.; Argulian, E.; Chan, L.; Dobbyn, A.; Guerraty, M. A.; Judy, R.; Kay, J.; Kember, R. L.; Levin, M. G.; Saha, A.; Van Vleck, T.; Verma, S. S.; Weaver, J.; Abul-Husn, N. S.; Baras, A.; Chirinos, J. A.; Drachman, B.; Kenny, E. E.; Loos, R. J. F.; Narula, J.; Overton, J.; Reid, J.; Ritchie, M.; Sirugo, G.; Nadkarni, G.; Rader, D. J.; Do, R. Association of the V122I hereditary transthyretin amyloidosis genetic variant with heart failure among individuals of african or hispanic/latino ancestry. *JAMA* **2019**, *322*, 2191-2202.

17.   Jiang, X.; Buxbaum, J. N.; Kelly, J. W. The V122I cardiomyopathy variant of transthyretin increases the velocity of rate-limiting tetramer dissociation, resulting in accelerated amyloidosis. *Proc. Natl. Acad. Sci. U S A* **2001**, *98*, 14943-14948.

18. Sousa, M. M.; Fernandes, R.; Palha, J. A.; Taboada, A.; Vieira, P.; Saraiva, M. J. Evidence for early cytotoxic aggregates in transgenic mice for human transthyretin Leu55Pro. *Am. J. Pathol.* **2002**, *161*, 1935-1948.

19. Kamata, M.; Susanto, M. T.; Chen, I. S. Enhanced transthyretin tetramer stability following expression of an amyloid disease transsuppressor variant in mammalian cells. *J. Gene. Med.* **2009**, *11*, 103-111.

20. Mathew, V.; Wang, A. K. Inotersen: new promise for the treatment of hereditary transthyretin amyloidosis. *Drug. Des. Devel. Ther.* **2019**, *13*, 1515-1525.

21. Hoy, S. M. Patisiran: first global approval. *Drugs* **2018**, *78*, 1625-1631.

22. Bulawa, C. E.; Connelly, S.; Devit, M.; Wang, L.; Weigel, C.; Fleming, J. A.; Packman, J.; Powers, E. T.; Wiseman, R. L.; Foss, T. R.; Wilson, I. A.; Kelly, J. W.; Labaudiniere, R. Tafamidis, a potent and selective transthyretin kinetic stabilizer that inhibits the amyloid cascade. *Proc. Natl. Acad. Sci. U S A* **2012**, *109*, 9629-9634.

23. Coelho, T.; Maia, L. F.; da Silva, A. M.; Cruz, M. W.; Plante-Bordeneuve, V.; Suhr, O. B.; Conceicao, I.; Schmidt, H. H.; Trigo, P.; Kelly, J. W.; Labaudiniere, R.; Chan, J.; Packman, J.; Grogan, D. R. Long-term effects of tafamidis for the treatment of transthyretin familial amyloid polyneuropathy. *J. Neurol.* **2013**, *260*, 2802-2814.

24. Coelho, T.; Merlini, G.; Bulawa, C. E.; Fleming, J. A.; Judge, D. P.; Kelly, J. W.; Maurer, M. S.; Plante-Bordeneuve, V.; Labaudiniere, R.; Mundayat, R.; Riley, S.; Lombardo, I.; Huertas, P. Mechanism of action and clinical application of tafamidis in hereditary transthyretin amyloidosis. *Neurol. Ther.* **2016**, *5*, 1-25.

25. Cruz, M. W. Tafamidis for autonomic neuropathy in hereditary transthyretin (ATTR) amyloidosis: a review. *Clin. Auton. Res.* **2019**, *29* (Suppl 1), 19-24.

26. Lamb, Y. N.; Deeks, E. D. Tafamidis: a review in transthyretin amyloidosis with polyneuropathy. *Drugs* **2019**, *79*, 863-874.

27. Park, J.; Egolum, U.; Parker, S.; Andrews, E.; Ombengi, D.; Ling, H. Tafamidis: a first-in-class transthyretin stabilizer for transthyretin amyloid cardiomyopathy. *Ann. Pharmacother.* **2020**, *54*, 470-477.

28. Alhamadsheh, M. M.; Connelly, S.; Cho, A.; Reixach, N.; Powers, E. T.; Pan, D. W.; Wilson, I. A.; Kelly, J. W.; Graef, I. A. Potent kinetic stabilizers that prevent transthyretin-mediated cardiomyocyte proteotoxicity. *Sci. Transl. Med.* **2011**, *3*, 97ra81.

29. Miller, M.; Pal, A.; Albusairi, W.; Joo, H.; Pappas, B.; Haque Tuhin, M. T.; Liang, D.; Jampala, R.; Liu, F.; Khan, J.; Faaij, M.; Park, M.; Chan, W.; Graef, I.; Zamboni, R.; Kumar, N.; Fox, J.; Sinha, U.; Alhamadsheh, M. Enthalpy-driven stabilization of transthyretin by AG10 mimics a naturally occurring genetic variant that protects from transthyretin amyloidosis. *J. Med. Chem.* **2018**, *61*, 7862-7876.

30. Penchala, S. C.; Connelly, S.; Wang, Y.; Park, M. S. Zhao, L.; Baranczak, A.; Rappley, I.; Vogel, H.; Liedtke, M.; Witteles, R. M.; Powers, E. T.; Reixach, N.; Chan, W. K.; Wilson, I. A.; Kelly, J. W.; Graef, I. A.; Alhamadsheh, M. M. AG10 inhibits amyloidogenesis and cellular toxicity of the familial amyloid cardiomyopathy-associated V122I transthyretin. *Proc. Natl. Acad. Sci. U S A* **2013**, *110*, 9992-9997.

31.   Maurer, M. S.; Schwartz, J. H.; Gundapaneni, B.; Elliott, P. M.; Merlini, G.; Waddington-Cruz, M.; Kristen, A. V.; Grogan, M.; Witteles, R.; Damy, T.; Drachman, B. M.; Shah, S. J.; Hanna, M.; Judge, D. P.; Barsdorf, A. I.; Huber, P.; Patterson, T. A.; Riley, S.; Schumacher, J.; Stewart, M.; Sultan, M. B.; Rapezzi, C. Investigators, A.-A. S., Tafamidis treatment for patients with transthyretin amyloid cardiomyopathy. *N. Engl. J. Med.* **2018**, *379*, 1007-1016.

32.   Judge, D. P.; Heitner, S. B.; Falk, R. H.; Maurer, M. S.; Shah, S. J.; Witteles, R. M.; Grogan, M.; Selby, V. N.; Jacoby, D.; Hanna, M.; Nativi-Nicolau, J.; Patel, J.; Rao, S.; Sinha, U.; Turtle, C. W.; Fox, J. C. Transthyretin stabilization by AG10 in symptomatic transthyretin amyloid cardiomyopathy. *J. Am. Coll. Cardiol.* **2019**, *74*, 285-295.

33.   Berk, J. L.; Suhr, O. B.; Obici, L.; Sekijima, Y.; Zeldenrust, S. R.; Yamashita, T.; Heneghan, M. A.; Gorevic, P. D.; Litchy, W. J.; Wiesman, J. F.; Nordh, E.; Corato, M.; Lozza, A.; Cortese, A. Robinson-Papp, J.; Colton, T.; Rybin, D. V.; Bisbee, A. B.; Ando, Y.; Ikeda, S.; Seldin, D. C.; Merlini, G.; Skinner, M.; Kelly, J. W.; Dyck, P. J. Diflunisal trial, C., repurposing diflunisal for familial amyloid polyneuropathy: a randomized clinical trial. *JAMA* **2013**, *310*, 2658-2667.

34.   Sant'Anna, R.; Gallego, P.; Robinson, L. Z.; Pereira-Henriques, A.; Ferreira, N.; Pinheiro, F.; Esperante, S.; Pallares, I.; Huertas, O.; Almeida, M. R.; Reixach, N.; Insa, R.; Velazquez-Campoy, A.; Reverter, D.; Reig, N.; Ventura, S. Repositioning tolcapone as a potent inhibitor of transthyretin amyloidogenesis and associated cellular toxicity. *Nat. Commun.* **2016**, *7*, 10787.
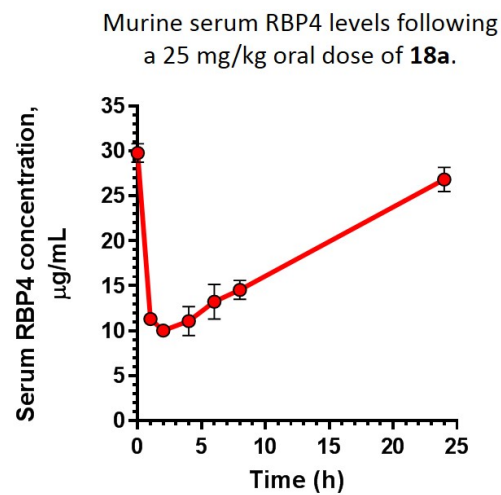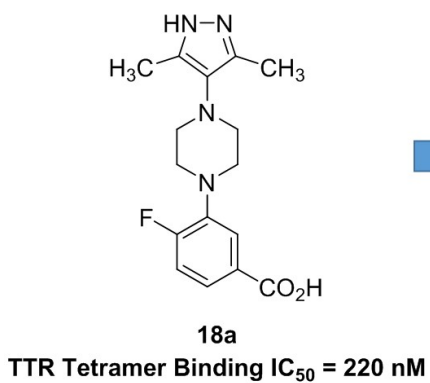
35. Vilaro, M.; Nieto, J.; La Parra, J. R.; Almeida, M. R.; Ballesteros, A.; Planas, A.; Arsequell, G.; Valencia, G. Tuning transthyretin amyloidosis inhibition properties of iododiflunisal by combinatorial engineering of the nonsalicylic ring substitutions. *ACS Comb. Sci.* **2015**, *17*, 32-38.

36. Almeida, M. R.; Macedo, B.; Cardoso, I.; Alves, I.; Valencia, G.; Arsequell, G.; Planas, A.; Saraiva, M. J. Selective binding to transthyretin and tetramer stabilization in serum from patients with familial amyloidotic polyneuropathy by an iodinated diflunisal derivative. *Biochem. J.* **2004**, *381(Pt 2)*, 351-356.

37. Wang, H.; Tang, Y.; Lei, M. Models for binding cooperativities of inhibitors with transthyretin. *Arch. Biochem. Biophys.* **2007**, *466*, 85-97.

38. Petrassi, H. M.; Johnson, S. M.; Purkey, H. E.; Chiang, K. P.; Walkup, T.; Jiang, X.; Powers, E. T.; Kelly, J. W. Potent and selective structure-based dibenzofuran inhibitors of transthyretin amyloidogenesis: kinetic stabilization of the native state *J. Am. Chem. Soc.* **2005**, *127*, 6662-6671.

39. Johnson, S. M.; Petrassi, H. M.; Palaninathan, S. K.; Mohamedmohaideen, N. N.; Purkey, H. E.; Nichols, C.; Chiang, K. P.; Walkup, T.; Sacchettini, J. C.; Sharpless, K. B.; Kelly, J. W. Bisaryloxime ethers as potent inhibitors of transthyretin amyloid fibril formation *J. Med. Chem.* **2005**, *48,* 1576-1587.

40. Radu, R. A.; Han, Y.; Bui, T. V.; Nusinowitz, S.; Bok, D.; Lichter, J.; Widder, K.; Travis, G. H.; Mata, N. L. Reductions in serum vitamin A arrest accumulation of toxic retinal fluorophores: a potential therapy for treatment of lipofuscin-based retinal diseases. *Invest. Ophthalmol. Vis. Sci.* **2005**, *46*, 4393-4401.

41. Cioffi, C. L.; Dobri, N.; Freeman, E. E.; Conlon, M. P.; Chen, P.; Stafford, D. G.; Schwarz, D. M.; Golden, K. C.; Zhu, L.; Kitchen, D. B.; Barnes, K. D.; Racz, B.; Qin, Q.; Michelotti, E.; Cywin, C. L.; Martin, W. H.; Pearson, P. G.; Johnson, G.; Petrukhin, K. Design, synthesis, and evaluation of nonretinoid retinol binding protein 4 antagonists for the potential treatment of atrophic age-related macular degeneration and Stargardt disease. *J. Med. Chem.* **2014**, *57*, 7731-7757.

42. Cioffi, C. L.; Racz, B.; Freeman, E. E.; Conlon, M. P.; Chen, P.; Stafford, D. G.; Schwarz, D. M.; Zhu, L.; Kitchen, D. B.; Barnes, K. D.; Dobri, N.; Michelotti, E.; Cywin, C. L.; Martin, W. H.; Pearson, P. G.; Johnson, G.; Petrukhin, K. Bicyclic [3.3.0]-octahydrocyclopenta[c]pyrrolo antagonists of retinol binding protein 4: potential treatment of atrophic age-related macular degeneration and stargardt disease. *J. Med. Chem.* **2015**, *58*, 5863-5888.

43. Cioffi, C. L.; Racz, B.; Varadi, A.; Freeman, E. E.; Conlon, M. P.; Chen, P.; Zhu, L.; Kitchen, D. B.; Barnes, K. D.; Martin, W. H.; Pearson, P. G.; Johnson, G.; Blaner, W. S.; Petrukhin, K. Design, synthesis, and preclinical efficacy of novel nonretinoid antagonists of retinol-binding protein 4 in the mouse model of hepatic steatosis. *J. Med. Chem.* **2019**, *62*, 5470-5500.

44. Racz, B.; Varadi, A.; Pearson, P. G.; Petrukhin, K. Comparative pharmacokinetics and pharmacodynamics of the advanced Retinol-Binding Protein 4 antagonist in dog and cynomolgus monkey. *PLoS One* **2020**, *15*, e0228291.

45. Racz, B.; Varadi, A.; Kong, J.; Allikmets, R.; Pearson, P. G.; Johnson, G.; Cioffi, C. L.; Petrukhin, K. A non-retinoid antagonist of retinol-binding protein 4 rescues

phenotype in a model of Stargardt disease without inhibiting the visual cycle. *J. Biol. Chem.* **2018**, *293*, 11574-11588.

46.   Dobri, N.; Qin, Q.; Kong, J.; Yamamoto, K.; Liu, Z.; Moiseyev, G.; Ma, J. X.; Allikmets, R.; Sparrow, J. R.; Petrukhin, K. A1120, a nonretinoid RBP4 antagonist, inhibits formation of cytotoxic bisretinoids in the animal model of enhanced retinal lipofuscinogenesis. *Invest. Ophthalmol. Vis. Sci.* **2013**, *54*, 85-95.

47.   Fox, J. C.; Hellawell, J. L.; Rao, S.; O'Reilly, T.; Lumpkin, R.; Jernelius, J.; Gretler, D.; Sinha, U. First-in-human study of AG10, a novel, oral, specific, selective, and potent transthyretin stabilizer for the treatment of transthyretin amyloidosis: a phase 1 safety, tolerability, pharmacokinetic, and pharmacodynamic study in healthy adult volunteers. *Clin. Pharmacol. Drug Dev.* **2020**, *9*, 115-129.

48.   Cioffi, C. L.; Muthuraman, P.; Raja, A.; Varadi, A.; Racz, B.; Petrukhin, K. Discovery of bispecific antagonists of retinol binding protein 4 that stabilize transthyretin tetramers: scaffolding hopping, optimization, and preclinical pharmacological evaluation as a potential therapy for two common age-related comorbidities. *J. Med. Chem.* **2020**, *63*, 11054-11084.

49.   Regan, S. L.; Maggs, J. L.; Hammond, T. G.; Lambert, C.; Williams, D. P.; Park, B. K. Acyl glucuronides: the good, the bad and the ugly. *Biopharm. Drug Dispos.* **2010**, *31*, 367-395.

50.   Baurle, S.; Nagel, J.; Peters, O.; Brauer, N.; Ter Laak, A.; Preusse, C.; Rottmann, A.; Heldmann, D.; Bothe, U.; Blume, T.; Zorn, L.; Walter, D.; Zollner, T. M.; Steinmeyer, A.; Langer, G. Identification of a benzimidazolecarboxylic acid

derivative (BAY 1316957) as a potent and selective human prostaglandin e2 receptor subtype 4 (hEP4-R) antagonist for the treatment of endometriosis. *J. Med. Chem.* **2019**, *62*, 2541-2563.

Table of Contents Graphic

18a
TTR Tetramer Binding IC$_{50}$ = 220 nM

Murine serum RBP4 levels following a 25 mg/kg oral dose of **18a**.

Maximal 66% reduction in serum RBP4 levels

Supporting Information

Identification of Transthyretin Tetramer Kinetic Stabilizers That Are Capable of Inhibiting the Retinol-Dependent Retinol Binding Protein 4-Transthyretin Interaction

Christopher L. Cioffi,*† Arun Raja,† Parthasarathy Muthuraman,† Aravindan Jayaraman,† Srinivasan Jayakumar,† Andras Varadi,§ Boglarka Racz,§ and Konstantin Petrukhin*§

†Albany College of Pharmacy and Health Sciences, Departments of Basic and Clinical Sciences and Pharmaceutical Sciences, 106 New Scotland Ave, Albany, NY 12208
§Department of Ophthalmology, Columbia University Medical Center, New York, NY 10032

Corresponding Authors

*Christopher L. Cioffi: phone, 518-694-7224; e-mail: christopher.cioffi@acphs.edu.
*Konstantin Petrukhin: phone, 212-305-9040; e-mail: kep4@cumc.columbia.edu.

Table of Contents

TTR *In Vitro* Assay Information

Fluorescence Polarization TTR Tetramer Binding Assay. Compound binding to TTR was assessed in the fluorescence polarization assay. The assay measured competitive displacement of the fluorescent probe, FITC-diclofenac, from TTR isolated from human plasma (Clabiochem-Millipore, cat. No. 52957). FITC-diclofenac was synthesized at LeadGen Labs, LLC following the published procedure. Each well contained 200 nM TTR and 100 nM FITC-diclofenac in the FP buffer (10 mM Tris-HCl pH 7.5, 150 mM NaCl, 0.01% CHAPS, 0.01% Prionex) along with test compounds. Nonspecific binding was determined in the presence of 500 μM unlabeled diclofenac (Sigma-Aldrich). Reactions with test compounds were incubated overnight at +4 ^{o}C and FP was measured on SpectramaxM5e plate reader (Molecular Devices).

TTR Aggregation Assay. The ability of test compounds to prevent TTR aggregation was evaluated under the acidic conditions that favor TTR aggregation and fibril formation. A 2 μl solution of 167 μM human TTR (ACROBiosystems #H5223) was incubated with 7 μl 50 mM sodium acetate pH 4.0 (Sigma # S7545), 100 mM KCl (Sigma # S5405) in the presence or absence of 1 μl TTR inhibitor for 72 h at 37 °C. At the end of the incubation, 3.5 μl 500 mM sodium phosphate (Sigma #S5136) buffer pH = 8.0 was added to each sample for neutralization and 0.6 μl 5% CHAPS (Sigma #C5070) as a detergent to prevent reassociation of protein. The cross-linking was performed by adding 1.5 μl 5% glutaraldehyde solution (Sigma# G6257). After 4 min, the reaction was stopped by the addition of 2.5 μl freshly made 5% NaBH4. Samples were subjected to TTR western blotting with prealbumin antibodies (1:500; Dako #A0002). Band intensity for TTR monomer and TTR aggregates was quantified from scanned images of the blots.

RBP4 *In Vitro* Assay Information

***In vitro* binding of compounds to RBP4.** Compound binding to RBP4 was assessed in the radiometric scintillation proximity (SPA) assay that was previously described. The assay measured competitive displacement of radiolabeled all-*trans*-retinol from native RBP4 purified from human urine (Fitzgerald, 30R-AR022L). The protein was biotinylated using the EZ-link Sulfo-NHS-LC-Biotinylation kit from ThermoFisher (Cat #21335) as recommended by the manufacturer. Binding assays were implemented in a final volume of 100 μL in SPA buffer (1 X PBS, pH 7.4, 1 mM EDTA, 0.1% BSA, 0.5% CHAPS). The assay reaction included a radioligand, 10 nM ^{3}H-retinol (48.7 Ci/mmol; PerkinElmer, Waltham, MA), along with the 0.3 mg/well Streptavidin-PVT beads (PerkinElmer, RPNQ0006) and 50 nM biotinylated human RBP4. Unlabeled all-*trans*-retinol (Sigma, cat # 95144) at 20 μM was added to control wells to assess a nonspecific binding. Radioactivity counts were measured using CHAMELEON plate reader (Hidex Oy, Turku, Finland) after 16 h of incubation at rt with mild shaking.

Assessment of antagonistic activity in the HTRF RBP4-TTR interaction assay. The ability of analogues to act as antagonists of all-*trans*-retinol-dependent RBP4-TTR interaction was

measured in the HTRF (Homogenous Time-Resolved Fluorescence) assay as we described previously.[18, 19, 26] Untagged TTR (Calbiochem, cat #529577) and Maltose-Binding Protein-tagged RBP4 expressed in *E. coli* were used in this assay. HTRF Cryptate labeling kit from CisBio (Cisbio, cat #62EUSPEA, Bedfored, MA) was used to label TTR with Eu^{3+} Cryptate. The assay was performed in a final assay volume of 16μl in the buffer that contained 10 mM Tris-HCl pH 7.5 , 1 mM DTT, 0.05% NP-40, 0.05% Prionex, 6% glycerol, and 400 mM KF. Other components of the reaction mix included 60 nM MBP-RBP4, 5 nM TTR-Eu, 26.7 nM of anti-MBP antibody conjugated with d2 (Cisbio, cat #61MBPDAA), and 1 μM all-*trans* retinol (Sigma, cat # 95144). All the reactions were performed under dim red light in the dark. The plates were read in the SpectraMax M5e Multimode Plate Reader (Molecular Devices, Sunnyvale, CA) after the overnight incubation at 4 $^{\circ}$C. Fluorescence was excited at 337 nm; emission was measured at 668 and 620 nm with 75 μs counting delay. The HTRF signal was expressed as the ratio of fluorescence intensity: Flu_{668}/Flu_{620} X 10,000.

Mouse PK Study Information and Data

Drug naïve adult male CD-1 mice were administered a single dose administration of the test article by intravenous (IV) or oral gavage (PO) dose routes.

Testing Facility and Test Site: Absorption Systems, LLC, 436 Creamery Way, Suite 600, Exton, PA 19341–2556.

TEST ARTICLE AND VEHICLE INFORMATION:

IV dosing vehicles: 3% DMA/45% PEG300/12% ethanol/40% sterile water

PO dosing vehicle: 2% Tween 80 in 0.9% saline

Dose formulation: The dose formulation was prepared by the step-wise addition (in the order listed) of the individual components of the vehicle to a weighed quantity of test compound in a volume that yielded the desired final concentration. Each formulation was prepared by mixing a weighed quantity of test compound with the appropriate volume of vehicle.

Dosing Solution
Analysis: The dosing solutions were analyzed by LC-MS/MS. The measured dosing solution concentrations are shown in Table 1. The dosing solutions were diluted into mouse blood and analyzed in triplicate. All concentrations are expressed as mg/mL of the free base. The nominal dosing level was used in all calculations for Group 1.

TEST SYSTEM:

Species and strain: mouse; male CD-1

Mean weight: 0.034 kg for the IV arm; 0.027 kg for PO arm

Number: 3 animals total (same three animals used for each dosing group (Group 1 (IV) and Group 2 (PO))

COMPLIANCE: This non-clinical study followed established practices and standard operating procedures of Absorption Systems as well as the study protocol. This study was exploratory in nature and was not conducted in accordance with the principles set forth in the United States Food and Drug Administration (FDA) Good Laboratory Practice (GLP) Regulations, 21 Code of Federal regulations (CFR) Part 58. The report is archived in a validated scientific data management system. Electronic signatures comply with the regulation 21 CFR Part 11.

EXPERIMENTAL DESIGN:

Blood was collected from mice at pre-dose and at 5, 15 and 30 min, and 1, 2, 4, 8, 12, 24, and 48 h post-dose. Hemolyzed blood samples were extracted by protein precipitation using acetonitrile. Following protein extraction with acetonitrile, compound levels were measured by LC-MS/MS. Pharmacokinetic parameters were calculated from the time course of the blood concentrations. Pharmacokinetic parameters were determined with Phoenix WinNonlin (v8.0) software using a non-compartmental model. The maximum blood concentrations (C_0) after IV dosing were estimated by extrapolation of the first two time points back to t = 0. The maximum blood concentration (C_{max}) and the time to reach maximum blood concentration (t_{max}) after PO dosing were observed from the data. The area under the time concentration curve (AUC) was calculated using the linear trapezoidal rule with calculation to the last quantifiable data point, and with extrapolation to infinity if applicable. Blood half-life ($t_{1/2}$) was calculated from 0.693/slope of the terminal elimination phase. Mean residence time, MRT, was calculated by dividing the area under the moment curve (AUMC) by the AUC. Clearance (CL) was calculated from dose/AUC. Steady-state volume of distribution (V_{ss}) was calculated from CL*MRT. Bioavailability was determined by dividing the individual dose normalized PO AUC∞ values by the average dose-normalized IV AUC∞ value. Any samples below the limit of quantitation (1.00 ng/mL) were treated as zero for pharmacokinetic data analysis.

Individual and average blood concentrations are shown in Supplementary Table 1 and Table 2. All data are expressed as ng/mL of the free base. Samples that were below the limit of quantification (1.00 ng/mL) were not used in the calculation of averages. Average concentrations versus time data are plotted in Figure S-1 and Figure S-2.

Supplementary Table S-1. Individual and average blood concentrations (ng/mL) and pharmacokinetic parameters for **18a** (ACPHS-14-2) after intravenous (IV) administration at 2 mg/kg in male CD-1 mice.

	Intravenous (2 mg/kg)				
Time (hr)	**Mouse #**				
	391	**392**	**393**	**Mean**	**SD**
0 (pre-dose)	BLOQ	BLOQ	BLOQ	ND	ND
0.083	1290	1210	1590	1363	200
0.25	937	868	1080	962	108
0.50	770	608	**936**	771	164
1.0	**620**	**468**	**596**	561	81.7
2.0	**460**	**304**	**464**	409	91.2
4.0	**333**	**208**	**532**	358	163
8.0	**278**	**178**	**445**	300	135
24	**27.0**	**8.49**	**23.6**	19.7	9.85
48	**1.91**	BLOQ	**2.00**	1.96	ND
Animal Weight (kg)	0.034	0.032	0.033	0.033	0.001
Volume Dosed (mL)	0.07	0.06	0.07	0.07	0.01
C_0 (ng/mL)^1	1512	1427	1927	1622	267
$t_{1/2}$ (hr)	5.68	4.15	5.41	5.08	0.814
MRT_{last} (hr)	6.82	5.08	6.62	6.18	0.955
CL (L/hr/kg)	0.322	0.506	0.234	0.354	0.139
V_{ss} (L/kg)	2.23	2.73	1.57	2.18	0.585
AUC_{last} (hr·ng/mL)	6205	3898	8540	6214	2321
AUC_∞ (hr·ng/mL)	6221	3949	8556	6242	2303
Dose-normalized Values^2					
AUC_{last} (hr·kg·ng /mL/mg)	3103	1949	4270	3107	1160
AUC_∞ (hr·kg·ng /mL/mg)	3110	1975	4278	3121	1152

C_0: maximum blood concentration extrapolated to t=0; t_{max}: time of maximum blood concentration; $t_{1/2}$: half-life, data points used for half-life determination are in bold; MRT_{last}: mean residence time, calculated to the last observable time point; CL: clearance; V_{ss}: steady state volume of distribution; AUC_{last}: area under the curve, calculated to the last observable time point; AUC_∞: area under the curve, extrapolated to infinity; ND: not determined; BLOQ: below the limit of quantitation (1.00 ng/mL).
[1]Extrapolated to t=0.
[2]Dose-normalized by dividing the parameter by the nominal dose in mg/kg.

Figure S-1. Average blood concentrations of **18a** (ACPHS-14-2) after IV administration at 2 mg/kg in male CD-1 mice.
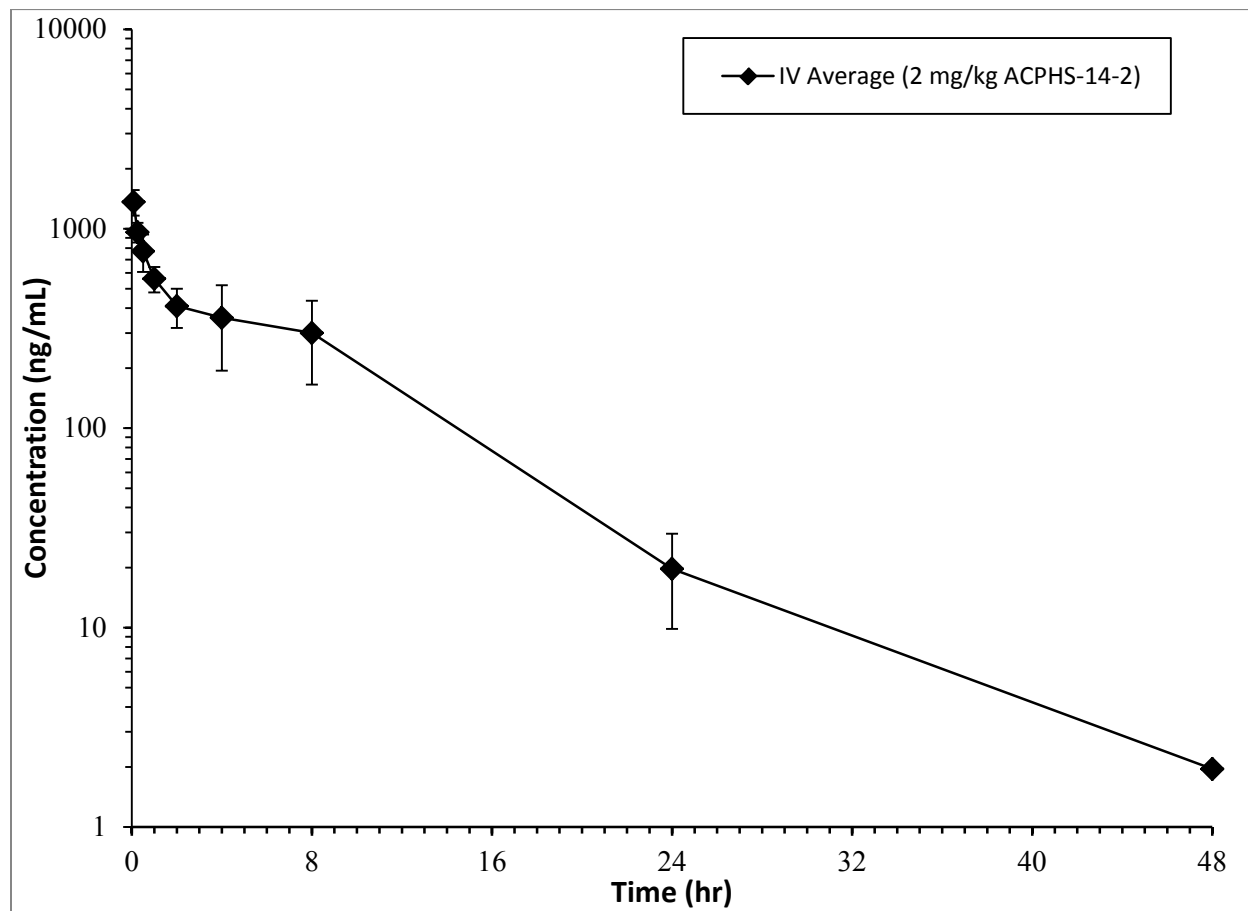
Supplementary Table S-2. Individual and average blood concentrations (ng/mL) and pharmacokinetic parameters for **18a** (ACPHS-14-2) after oral (PO) administration at 5 mg/kg in male CD-1 mice.

	Oral (5 mg/kg)				
	Mouse #				
Time (hr)	394	395	396	Mean	SD
0 (pre-dose)	BLOQ	BLOQ	BLOQ	ND	ND
0.25	1560	1310	1450	1440	125
0.50	**1370**	1450	1680	1500	161
1.0	**1350**	1310	**1560**	1407	134
2.0	**988**	257	**1340**	862	552
4.0	**1060**	**973**	**1170**	1068	98.7
8.0	**821**	**719**	**987**	842	135
24	**77.4**	**35.6**	**51.0**	54.7	21.1
48	**6.90**	**2.58**	**3.00**	4.16	2.38
Animal Weight (kg)	0.030	0.030	0.032	0.031	0.001
Volume Dosed (mL)	0.15	0.15	0.16	0.15	0.01
C_{max} (ng/mL)	1560	1450	1680	1563	115
t_{max} (hr)	0.25	0.50	0.50	0.42	0.14
$t_{1/2}$ (hr)	6.10	4.99	5.04	5.38	0.624
MRT_{last} (hr)	7.54	6.87	6.71	7.04	0.444
AUC_{last} (hr·ng/mL)	16419	13091	18609	16040	2778
AUC_{∞} (hr·ng/mL)	16480	13110	18630	16073	2783
Dose-normalized Values[1]					
AUC_{last} (hr·kg·ng /mL/mg)	3284	2618	3722	3208	556
AUC_{∞} (hr·kg·ng /mL/mg)	3296	2622	3726	3215	557
Bioavailability (%)[2]	106	84.0	119	103	17.8

C_{max}: maximum blood concentration; t_{max}: time of maximum blood concentration; $t_{1/2}$: half-life, data points used for half-life determination are in bold; MRT_{last}: mean residence time, calculated to the last observable time point; AUC_{last}: area under the curve, calculated to the last observable time point; AUC_{∞}: area under the curve, extrapolated to infinity; ND: not determined; BLOQ: below the limit of quantitation (1.00 ng/mL).
[1]Dose-normalized by dividing the parameter by the nominal dose in mg/kg.
[2]Bioavailability determined by dividing the individual dose-normalized oral AUC_{∞} values by the average dose-normalized IV AUC_{∞} value.

Figure S-2. Average blood concentrations of **18a** (ACPHS-14-2) after PO administration at 5 mg/kg in male CD-1 mice.
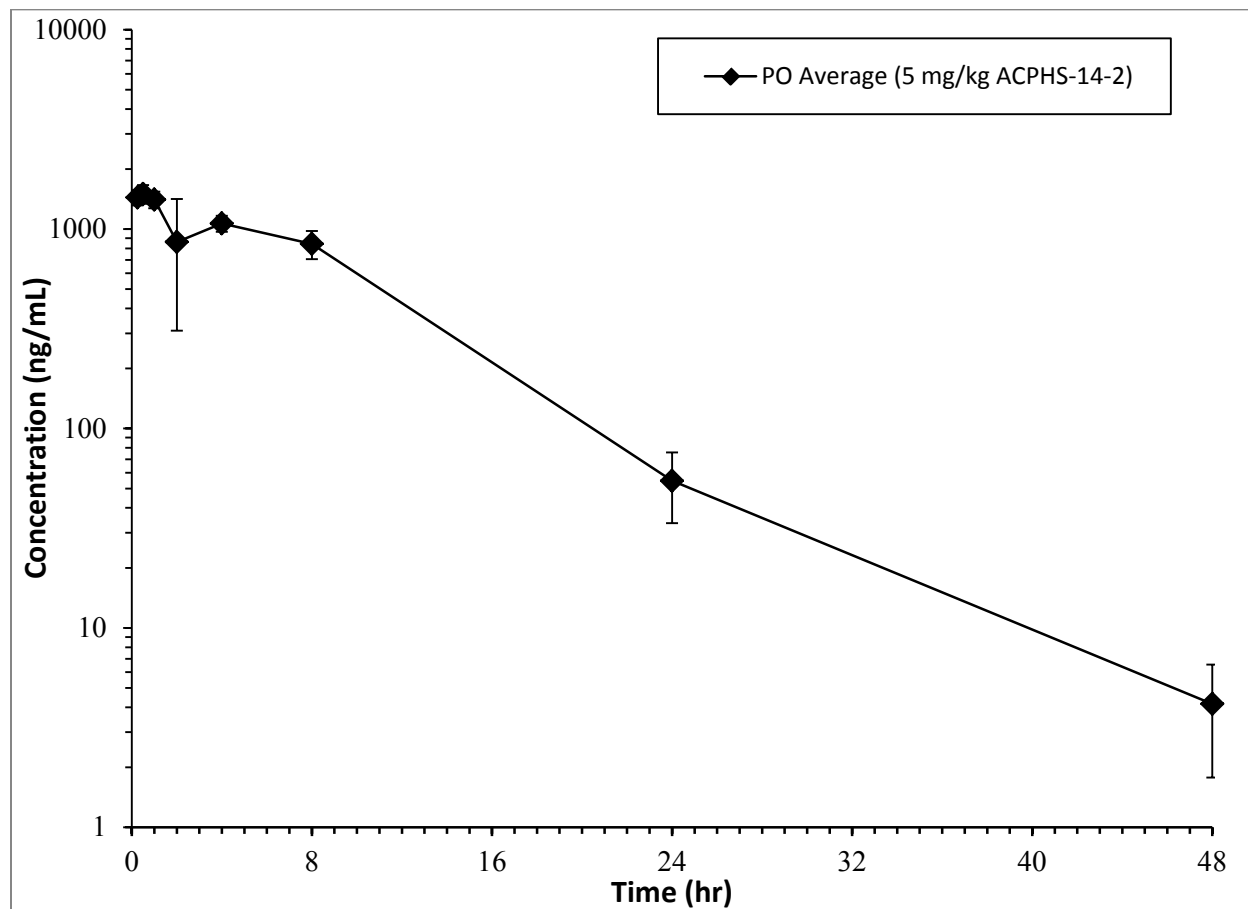
Animal Care and Use Statement: All procedures in this protocol are in compliance with the U.S. Department of Agriculture's (USDA) Animal Welfare Act (9 CFR Parts 1, 2, and 3); the Guide for the Care and Use of Laboratory Animals, Institute of Laboratory Animal Resources, National Academy Press, Washington, D.C., 1996; and the National Institutes of Health, Office of Laboratory Animal Welfare. Whenever possible, procedures in this study are designed to avoid or minimize discomfort, distress, and pain to animals.

Compliance: This non-clinical study followed established practices and standard operating procedures of Absorption Systems as well as the study protocol. This study was exploratory in nature and was not conducted in accordance with the principles set forth in the United States Food and Drug Administration (FDA) Good Laboratory Practice (GLP) Regulations, 21 Code of Federal regulations (CFR) Part 58. The report is archived in a validated scientific data management system. Electronic signatures comply with the regulation 21 CFR Part 11.

Serum RBP4 Measurement Information

Blood samples were collected from a tail vein. Whole blood was drawn into a centrifuge tube and was allowed to clot at rt for 30 min followed by centrifugation at 2000g for 15 min at 48 °C to collect serum. Aliquots of plasma samples collected in the mouse pharmacokinetic study were analyzed for the RBP4 concentration using the RBP4 (mouse/rat) dual ELISA kit (AdipoGen, San Diego, CA) following the manufacturer's instructions. In adi-hRBP4 transgenic mouse experiments, blood samples were collected from a tail vein. Whole blood was drawn into a centrifuge tube and was allowed to clot at rt for 30 min followed by centrifugation at 2000g for 15 min at +4 °C to collect serum. Mouse serum RBP4 (produced predominantly in the liver) was measured using the RBP4 (mouse/rat) dual ELISA kit (AdipoGen, San Diego, CA; catalog number AG-45A-0012YTP-KI01)

Animal Care and Use Statement: All procedures in this protocol are in compliance with the U.S. Department of Agriculture's (USDA) Animal Welfare Act (9 CFR Parts 1, 2, and 3); the Guide for the Care and Use of Laboratory Animals, Institute of Laboratory Animal Resources, National Academy Press, Washington, D.C., 1996; and the National Institutes of Health, Office of Laboratory Animal Welfare. Whenever possible, procedures in this study are designed to avoid or minimize discomfort, distress, and pain to animals.

In Vitro ADME Assay Information

Solubility

Kinetic Solubility in PBS:
Kinetic aqueous solubility determination for compound **18a** in PBS (pH 7.4) was conducted by Eurofins using UV detection (230 nm). Aqueous solubility (μM) was determined by comparing the peak area of the principal peak in a calibration standard (200 μM) containing organic

solvent (methanol/water, 60/40, v/v) with the peak area of the corresponding peak in a buffer sample. In addition, chromatographic purity (%) was defined as the peak area of the principal peak relative to the total integrated peak area in the HPLC chromatogram of the calibration standard. A chromatogram of the calibration standard of each test compound, along with a UV/VIS spectrum with labeled absorbance maxima, was generated.

Standards for the kinetic solubility study:

Metoprolol - 192.6 µM
Rifampicin - 200 µM
Ketoconazole - 152.8 µM
Phenytoin - 101.8 1 µM
Simvastatin - 14.2 µM
Diethylstilbesterol - 7.0 µM
Tamoxifen - 1.9 µM

CYP450 Inhibition

Inhibition potential (IC_{50} values) results for compound **18a** against the human cytochrome P450 (CYP) isoforms 2C9, 2C19, 2D6, and 3A4. Each recombinant human CYP isoform was tested with a standard positive and negative control, using fluorometric detection for measuring CYP activity. The measured IC_{50} values for the respective standard inhibitors were all within expected ranges for each isoform (see below).

IC_{50} Concentrations of Standard CYP Inhibitors:
CYP Inhibitor IC_{50} (µM):
2C9 Sulfaphenazole IC_{50} = 3.4 µM
2C19 Tranylcypromine IC_{50} = 2.8 µM
2D6 Quinidine IC_{50} = 0.058 µM
3A4 Ketoconazole IC_{50} = 0.0084 µM

Pre-formulated NADPH regenerating solutions, recombinant CYP isoforms 2C19 and 3A4 (Lot # 3007790 and 2276593 respectively), 3-[2-(N,N-diethyl-N-methylamino)ethyl]-7-methoxy-4-methylcoumarin (AMMC), 3-cyano-7-ethoxycoumarin (CEC) and 7-benzyloxy-4-trifluoromethylcoumarin (BFC) were obtained from Corning Life Sciences (Bedford, MA). Recombinant CYP isoform 2D6 (Lot # 49242) was obtained from Invitrogen (Carlsbad, CA). CYP isoform 2C9 (Lot # 0446966-1) was obtained from Cayman Chemical (Ann Arbor, MI). 7-methoxy-4-trifluoromethylcoumarin (MFC), trans-2-phenylcyclopropylamine HCl (TCP), sulfaphenazole (SFZ), ketoconazole (KTZ) and quinidine (QDN) were obtained from Sigma (St. Louis, MO). All solvents and buffers were obtained from commercial sources and used without further purification.

Methods:

Test compound was prepared as a 10 mM stock solution in acetonitrile. Four human P450 isoforms cDNA-expressed in insect cell microsomes (CYP2C9, CYP2C19, CYP2D6, and CYP3A4) were tested for inhibition by test compound using fluorescence-based assays. Nine serial dilutions (concentrations from 0–100 µM) using each test compound stock solution were prepared in black microtiter plates, in duplicate. This dilution series was incubated at 37 °C with the individual CYP isoforms and a standard fluorogenic probe substrate for each respective isoform. The concentration of the probe substrate added was at or near the Km value for each CYP isoform. Reaction mixtures contained potassium phosphate buffer, pH 7.4 and the NADPH-regenerating system. The final reaction volume was 0.20 mL and the reaction was terminated with 75 µL of stop solution (0.5 M Tris base in acetonitrile) after the appropriate incubation time (15-45 min). Fluorescence measurements were made at the appropriate excitation and emission wavelengths. Duplicate control wells with no test compound, duplicate blank wells containing stop solution prior to adding isoform, and a dilution series in duplicate containing a standard inhibitor for each isoform were also conducted. IC_{50} values were calculated using a non-linear regression of the data using the four-parameter logistic model (dose response equation) fit with XLFit 5.2 from IDBS Software (Emeryville, CA), supported by linear interpolation of data points at concentrations indicating inhibition levels approximately 50% of the uninhibited rate.

% Plasma Protein Binding

Plasma protein binding (PPB) for compounds determination for compound **18a** in PBS (pH 7.4) was conducted by Eurofins using equilibrium dialysis of plasma with HPLC-UV/Vis detection.

Mean Plasma Protein Binding of Control Propranolol in Human, Rat (Sprague Dawley), Mouse (CD-1), and Dog (Beagle) Plasma

The peak areas of the test compound in the buffer and test samples were used to calculate percent binding and recovery according to the following formulas:

$$\text{Protein binding(\%)} = \frac{Area_p - Area_b}{Area_p} * 100$$

$$\text{Recovery(\%)} = \frac{Area_p + Area_b}{Area_c} * 100$$

Where:
$Area_p$ = Peak area of analyte in protein matrix
$Area_b$ = Peak area of analyte in buffer
$Area_c$ = Peak area of analyte in control sample

Metabolic Stability

Metabolic Stability in Microsomes
The results of metabolic stability determinations for novel compounds and testosterone (positive control) were conducted in the presence of human, rat, mouse, and monkey liver microsomes. Values shown are percent of parent remaining after a 30 min incubation. All measurements were done in duplicate. Assay results for testosterone were within an acceptable range.

Metabolic Clearance in Microsomes
Mixed-gender human liver microsomes (Lot# 1710084), male Sprague-Dawley rat liver microsomes (Lot# 1610290), male CD-1 mouse liver microsomes (Lot# 1710069), and male Cynomolgous liver microsomes (Lot# 1510193) were purchased from XenoTech. The reaction mixture, minus NADPH, was prepared as described below. The test article was added into the reaction mixture at a final concentration of 1 µM. The control compound, testosterone, was run simultaneously with the test article in a separate reaction. An aliquot of the reaction mixture (without cofactor) was equilibrated in a shaking water bath at 37 °C for 3 min. The reaction was initiated by the addition of cofactor, and the mixture was incubated in a shaking water bath at 37 °C. Aliquots (100 µL) were withdrawn at 0, 10, 20, 30, and 60. Test article and testosterone samples were immediately combined with 400 µL of ice-cold 50/50 acetonitrile (ACN)/H2O containing 0.1% formic acid and internal standard to terminate the reaction. The samples were then mixed and centrifuged to precipitate proteins. All samples were assayed by LC-MS/MS using electrospray ionization. The peak area response ratio (PARR) to internal standard was compared to the PARR at time 0 to determine the percent remaining at each time point. Half-lives were calculated using GraphPad software, fitting to a single-phase exponential decay equation.

Supplementary Table S-3. Metabolic Clearance of **18a** in Human, Rat, Mouse, and Monkey Microsomes

Compound	Human		Rat		Mouse		Monkey	
	$t_{1/2}$ (min)	Microsomal CL$_{int}$ (µL/min/mg)	$t_{1/2}$ (min)	Microsomal CL$_{int}$ (µL/min/mg)	$t_{1/2}$ (min)	Microsomal CL$_{int}$ (µL/min/mg)	$t_{1/2}$ (min)	Microsomal CL$_{int}$ (µL/min/mg)
18a	>60	<0.0231	>60	<0.0231	>60	<0.0231	>60	<0.0231
Testosterone	19	0.0742	1.4	0.987	4.9	0.285	6.4	0.217

Intrinsic clearance (CL$_{int}$) was calculated based on CL$_{int}$ = k/P, where k is the elimination rate constant and P is the protein concentration in the incubation.

General Chemistry Information

General Chemistry. All reactions were performed under a dry atmosphere of nitrogen unless otherwise specified. Indicated reaction temperatures refer to the reaction bath, while room temperature (rt) is noted as 25 °C. Commercial grade reagents and anhydrous solvents were used as received from vendors and no attempts were made to purify or dry these components further. Removal of solvents under reduced pressure was accomplished with a Buchi rotary evaporator at approximately 28 mm Hg pressure using a Teflon-linked KNF vacuum pump. Thin layer chromatography was performed using 1" x 3" AnalTech No. 02521 silica gel plates with fluorescent indicator. Visualization of TLC plates was made by observation with either short wave UV light (254 nm lamp), 10% phosphomolybdic acid in ethanol or in iodine vapors. Preparative thin layer chromatography was performed using Analtech, 20 × 20 cm, 1000 micron preparative TLC plates. Flash column chromatography was carried out using a Teledyne Isco CombiFlash Companion Unit and a Biotage® Selekt System with Teledyne Isco RediSep Rf and Biotage Sfär silica gel columns. If needed, products were purified by reverse phase chromatography, using a Teledyne Isco CombiFlash Companion Unit and a Biotage® Selekt System with a RediSep Gold C18 reverse phase column. Proton NMR spectra were obtained on a 400 MHz Varian nuclear magnetic resonance spectrometer. Chemical shifts (δ) are reported in parts per million (ppm) and coupling constant (*J*) values are given in Hz, with the following spectral pattern designations: s, singlet; d, doublet; t, triplet, q, quartet; quint, quintet; m, multiplet; dd, doublet of doublets; dt, doublet of triplets; dq; doublet of quartets; br, broad signal. Tetramethylsilane was used as an internal reference. Peak listing, multiplicity designations, and coupling constant calculations were conducted using Mnova v.14 software (Mestrelab Research). Carbon NMR spectra were obtained on a 500 MHz Bruker AV III nuclear magnetic resonance spectrometer and tetramethylsilane was used as an internal reference. Fluorine NMR spectra were obtained on a 400 MHz Bruker AV III nuclear magnetic resonance spectrometer. Any melting points provided are uncorrected and were obtained using a Stanford Research Systems OptiMelt melting point apparatus (MPA100) with an automated melting point system. Mass spectroscopic analyses were performed using ESI ionization on a Waters AQUITY UPLC MS triple quadrapole mass spectrometer. High pressure liquid chromatography (HPLC) purity analysis was performed using a Waters Breeze2 HPLC system with a binary solvent system A and B using a gradient elusion [A, H_2O with 0.1% formic acid; B, CH_3CN with 0.1% formic acid] and flow rate = 0.5 mL/min, with UV detection at 254 nm (system equipped with a photodiode array (PDA) detector). An ACQUITY UPLC BEH C18 column, 130 Å, 1.7 μm, 2.1 mm × 50 mm was used. High resolution mass spectrometry (HRMS) analysis was was performed using an Agilent 6530 Accurate-Mass Q-TOF. All final compounds tested for *in vitro* and *in vivo* biological testing were purified to ≥95% purity, and these purity levels were measured by both ^{1}H NMR and HPLC.

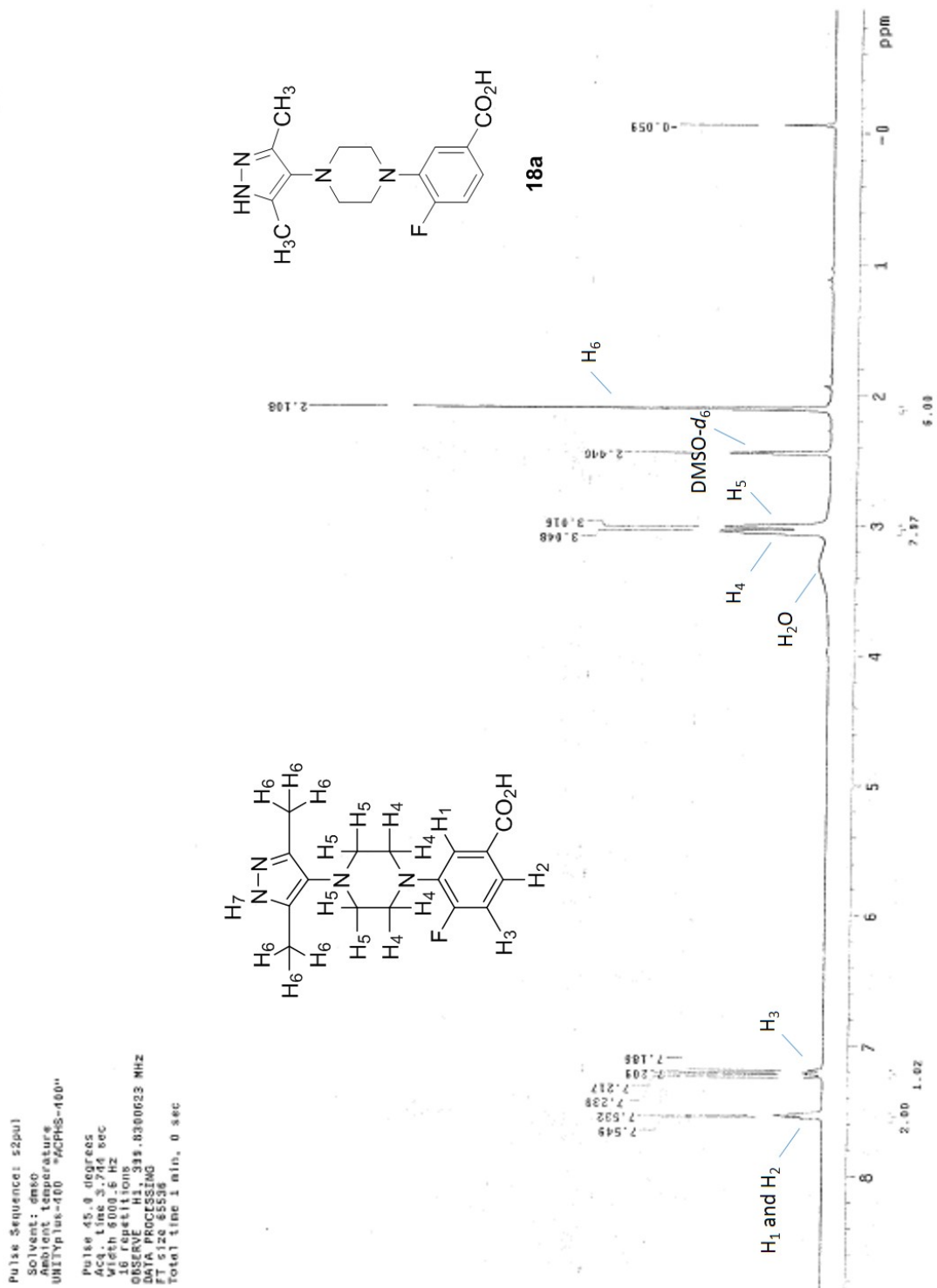**Figure S-3.** ^{1}H NMR (400 MHz, DMSO-d_6) Spectrum and Proton Assignment of Analogue **18a**

Figure S-4. ^{13}C NMR (500 MHz, DMSO-d_6) Spectrum of Analogue **18a**
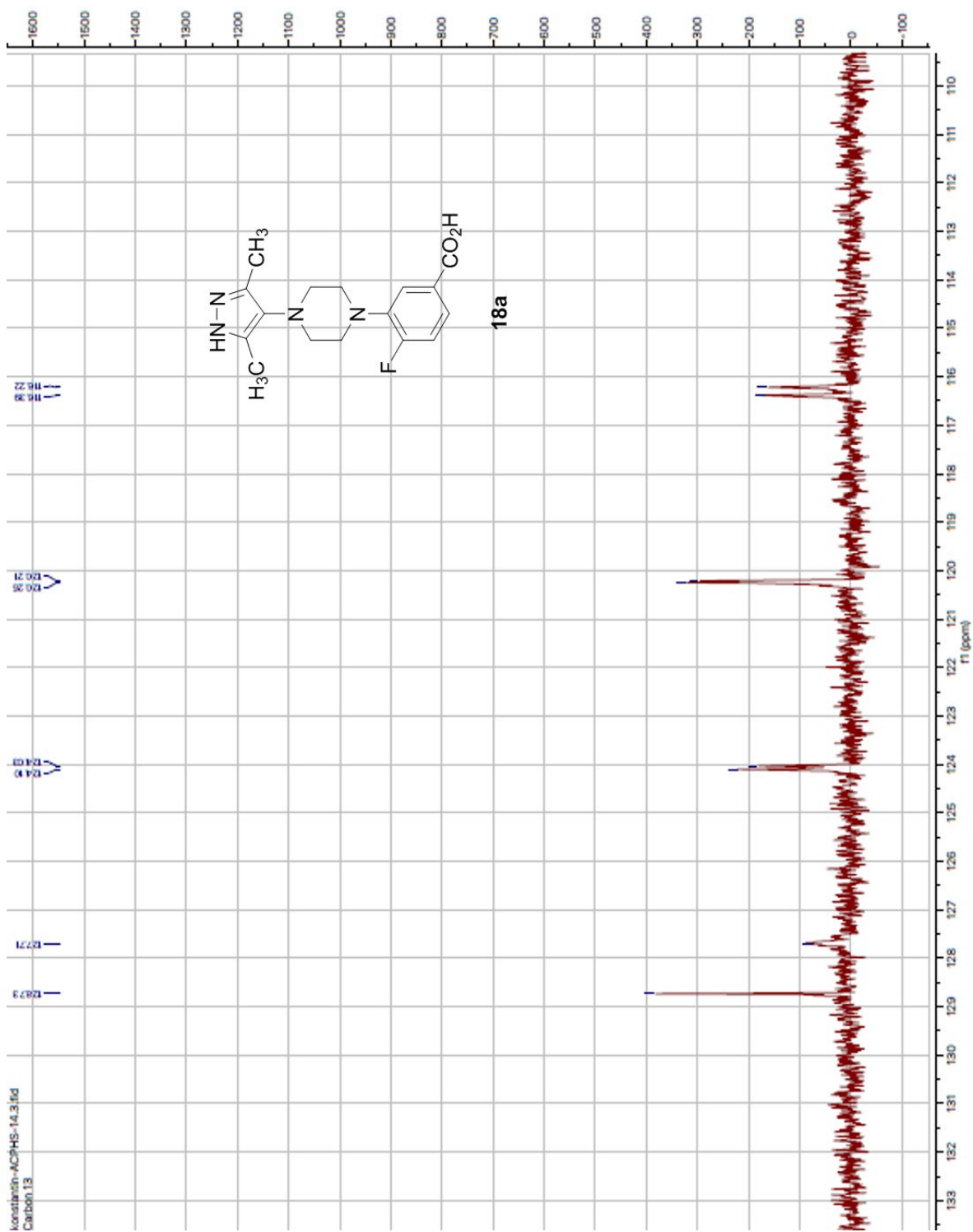
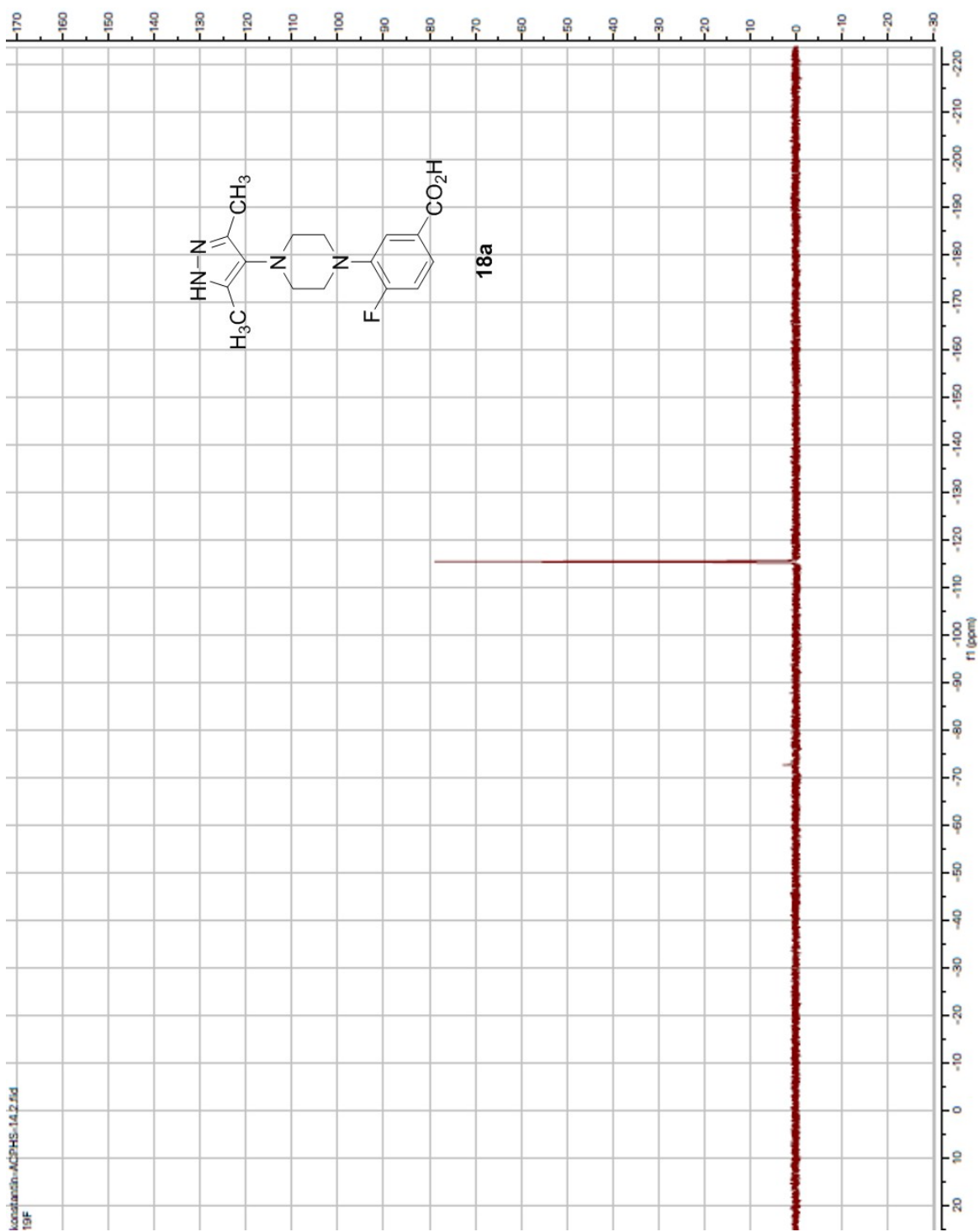**Figure S-5.** ^{19}F NMR (400 MHz, DMSO-d_6) Spectrum of Analogue **18a**

Figure S-6. ESI MS Analysis for Analogue **18a**

Sample Name: MPS-B-145-1	Acquired by: M. Parthasarathy, Ph.D.
Date Acquired: 07/11/2018	Principal Investigator: Dr. Christopher L Cioffi, Ph.D.

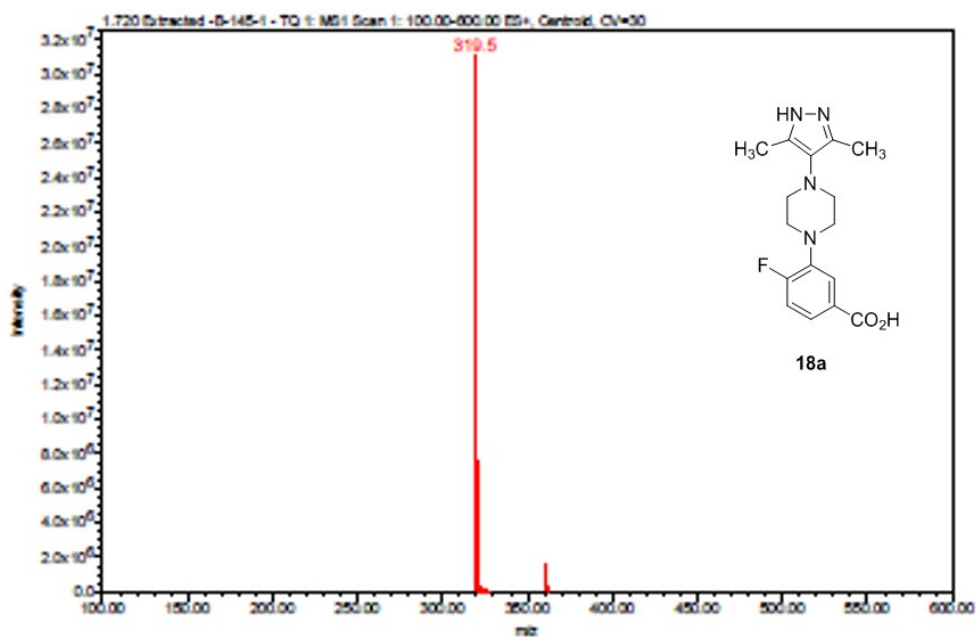| Instrument Model	ACQUITY UPLC®
Column	ACQUITY UPLC BEH C18 Column, 130Å, 1.7 μm, 2.1 mm X 50 mm
Mobile Phase :	
Aqueous Reservoir (A)	0.1% Formic acid in Water
Organic Reservoir (B)	0.1% Formic acid in ACN
Flow rate	0.5 mL/min
Injection volume	5 μL
Run Time	5 min
Wave length	UV= 254 nm

Mass Spectra (ES+):

Figure S-7. ESI HRMS Analysis for Analogue **18a**

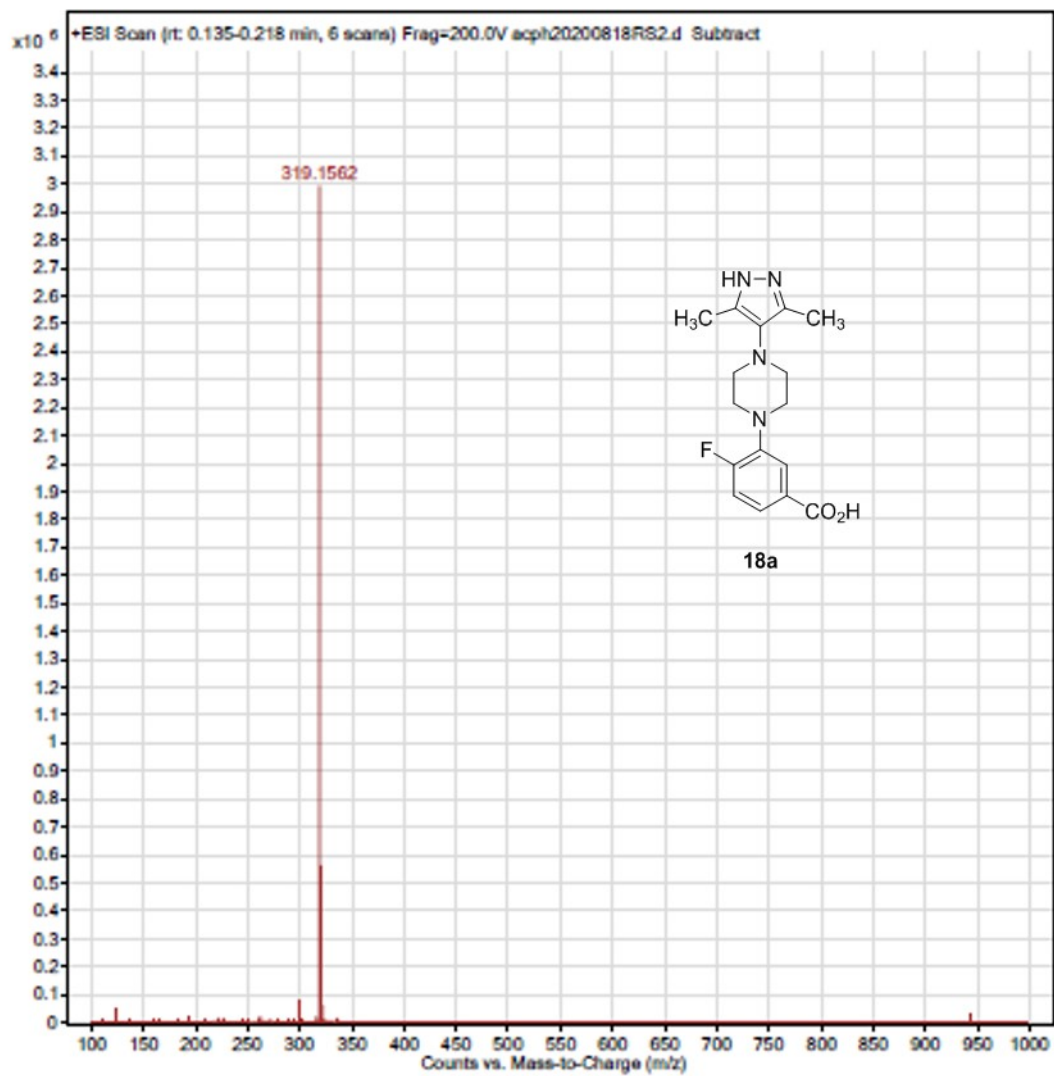**Figure S-8.** HPLC Chromatogram Analysis of Analogue **18a**

Sample Name: MPS-B-145-1		Acquired by: M. Parthasarathy, Ph.D.		
Date Acquired: 07/11/2018		Principal Investigator: Dr. Christopher L Cioffi, Ph.D.		

Instrument Model	Breeze™ 2 HPLC	HPLC gradient program:		
Column	XBridge BEH HILIC C18, 4.6 X 150 mm, 5 µm			
Mobile Phase :		Time (min)	%A	%B
Aqueous Reservoir (A)	0.25% TFA in Water	0.01	95	5
Organic Reservoir (B)	0.25% TFA in ACN	3.0	95	5
Flow rate	1.0 mL/min	13.0	5	95
Injection volume	5 µL	18.0	5	95
Run Time	30 min	22.0	95	5
Wave length	UV- 220 nm	25.0	Stop	

LC chromatogram:
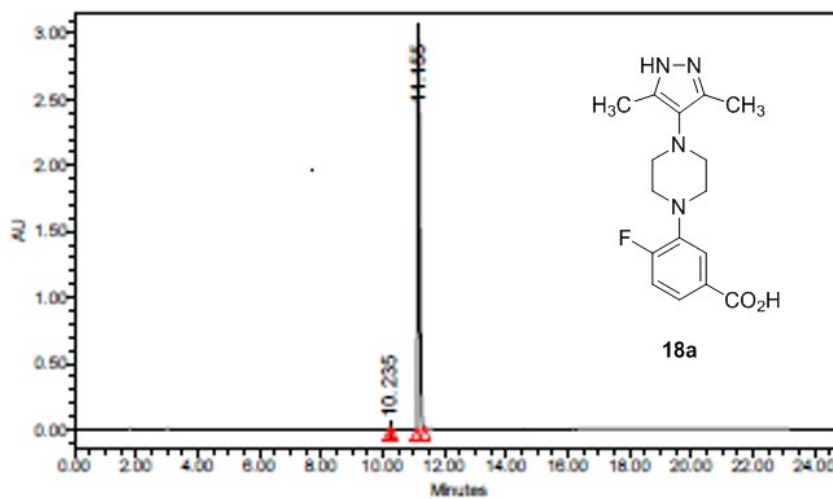
	Name	Retention Time	Area	% Area	Height
1		10.235	14932	0.10	5796
2		11.155	14558105	99.90	2997772

Supplementary Table S-4. SMILES Strings for Biologically Tested Compounds

Compound	SMILES
18a	CC1=C(C(C)=NN1)N2CCN(C3=C(F)C=CC(C(O)=O)=C3)CC2
18b	CC1=C(C(C)=NN1)N2CCN(C3=CC=CC(C(O)=O)=C3)CC2
18c	CC1=C(C(C)=NN1)N2CCN(C3=C(OC)C=CC(C(O)=O)=C3)CC2
18d	CC1=C(C(C)=NN1)N2CCN(C3=C(C)C=CC(C(O)=O)=C3)CC2
18e	CC1=C(C(C)=NN1)N2CCN(C3=C(C(F)(F)F)C=CC(C(O)=O)=C3)CC2
18f	CC1=C(C(C)=NN1)N2CCN(C3=C(Cl)C=CC(C(O)=O)=C3)CC2
18g	CC1=C(C(C)=NN1)N2CCN(C3=CC=CC(C(O)=O)=C3F)CC2
18h	CC1=C(C(C)=NN1)N2CCN(C3=CC=C(F)C(C(O)=O)=C3)CC2
18i	CC1=C(C(C)=NN1)N2CCN(C3=CC(F)=CC(C(O)=O)=C3)CC2
18j	CC1=C(C(C)=NN1)N2CCN(C3=C(F)C=CC(C(O)=O)=C3C)CC2
18k	CC1=C(C(C)=NN1)N2CCN(C3=C(F)C=C(C)C(C(O)=O)=C3)CC2
19	[H][C@]12CN(C3=C(F)C=CC(C(O)=O)=C3)C[C@@]1([H])CN(C4=C(C)NN=C4C)C2
(±)-20	FC(C=CC(C(O)=O)=C1)=C1N2CCC3(CN(C4=C(C)NN=C4C)CC3)C2
21	CC1=NNC(C)=C1N2CC3(CN(C4=C(F)C=CC(C(O)=O)=C4)C3)C2
23	FC(C=CC(C(O)=O)=C1)=C1N2CCN(C3=C(C)ON=C3C)CC2
25	FC(C=CC(C(O)=O)=C1)=C1N2CCN(C3=NNN=N3)CC2
27	FC(C=CC(C(O)=O)=C1)=C1N2CCN(C3=C(C(F)(F)F)C=CC=C3)CC2
29	FC(C=CC(C(O)=O)=C1)=C1N2CCN(CC3=CNN=C3C)CC2
30	CC1=C(C(C)=NN1)N(CC2)CCN2C3=C(F)C=CC(C(N)=O)=C3
31	CC1=C(C(C)=NN1)N(CC2)CCN2C3=C(F)C=CC(C4=NNN=N4)=C3